Nano Research

ISSN 1998-0124 CN 11-5974/O4
https://doi.org/10.26599/NR.2026.94908914

Research Article

"Dual-side shielding": Bromide additives enabling robust four-electron aqueous Zn–I_2 batteries

Zhenbang Zhuang[1,2], Jun Guo[2], Chunling Chen[2,3], Junmin Yan[1], Gang Huang[2,3](✉), Xinbo Zhang[2,3](✉)

[1] Key Laboratory of Automobile Materials, Ministry of Education, Department of Materials Science and Engineering, Jilin University, Changchun 130022, China

[2] China-Belarus Belt and Road Joint Laboratory on Advanced Materials and Manufacturing, Changchun Institute of Applied Chemistry, Chinese Academy of Sciences, Changchun 130022, China

[3] School of Applied Chemistry and Engineering, University of Science and Technology of China, Hefei 230026, China

Nano Res., **Just Accepted Manuscript** • https://doi.org/10.26599/NR.2026.94908914

https://www.sciopen.com/journal/1998-0124 on Jun. 6, 2026

Just Accepted

TABLE OF CONTENTS (TOC)

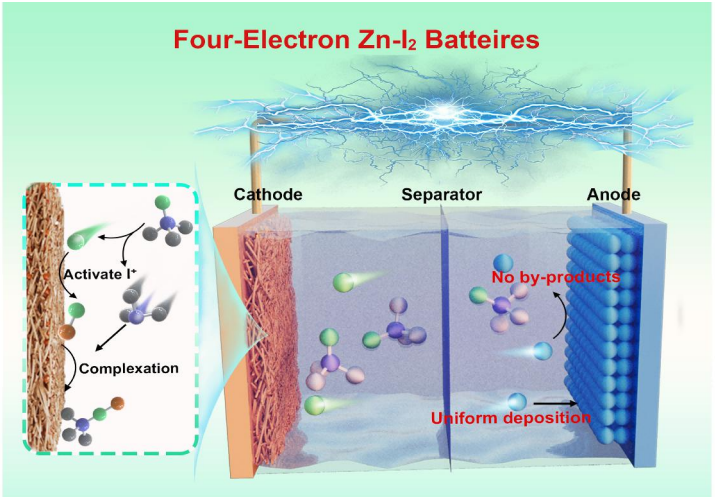

Trimethylammonium bromide (TMBr) with bidirectional regulation capability of cations and anions has been selected as a new type of bromide electrolyte additives to boost the performance of Zn–I_2 batteries. Its dual-side shielding functions for both electrodes enable the reversible four-electron I_2 transfer chemistry and long-term running of Zn–I_2 batteries

Nano Research

Open Access

Research Article

"Dual-side shielding": Bromide additives enabling robust four-electron aqueous Zn–I_2 batteries

Zhenbang Zhuang[1,2], Jun Guo[2], Chunling Chen[2,3], Junmin Yan[1], Gang Huang[2,3] ✉, and Xinbo Zhang[2,3] ✉

[1] *Key Laboratory of Automobile Materials, Ministry of Education, Department of Materials Science and Engineering, Jilin University, Changchun 130022, China*

[2] *China-Belarus Belt and Road Joint Laboratory on Advanced Materials and Manufacturing, Changchun Institute of Applied Chemistry, Chinese Academy of Sciences, Changchun 130022, China*

[3] *School of Applied Chemistry and Engineering, University of Science and Technology of China, Hefei 230026, China*

Received: 15 April 2026; **Revised:** 24 May 2026; **Accepted:** 6 June 2026

✉ Address correspondence to Gang Huang, ghuang@ciac.ac.cn; Xinbo Zhang, xbzhang@ciac.ac.cn

Cite this article: *Nano Research*, 2026, 19, 94908914 https://doi.org/10.26599/NR.2026.94908914

ABSTRACT: Aqueous Zn–I_2 batteries based on four-electron conversion chemistry have been extensive explored due to their high voltage and large specific capacity. However, the intrinsic instability of I^+ generated during the high-voltage conversion process and the severe electrochemical corrosion of Zn anode in aqueous electrolyte primarily hinder the construction of high-performance Zn–I_2 batteries. Herein, trimethylammonium bromide (TMBr) with functional cation and anion has been selected as a dual-side shielding electrolyte additive to concurrently resolve these problems. On the one hand, Br^- in TMBr could incorporate into the electrolyte solvation structure and reconstitute the hydrogen-bond (H-bond) network, suppressing the activity of free H_2O molecules and consequently enhancing the Zn anode stability. On the other hand, the Br^- could electrochemically activate I^+, followed by the stabilization of I^+ via complexation interactions with trimethylamine cations (TM^+) and Br^-, synergistically achieving facile high-voltage conversion chemistry of I_2 cathode. As a result, the TMBr additive enables the four-electron conversion-type Zn–I_2 batteries to demonstrate a remarkable capacity of 250 mAh g^{-1} coupled with stable cycling exceeding 15000 cycles at 3 A g^{-1}. Additionally, the 160 mAh pouch cell delivers an energy density of 367.4 Wh kg^{-1} (based on I_2 mass) with a lifetime of over 300 cycles.

KEYWORDS: aqueous Zn–I_2 batteries, four-electron conversion, electrolyte additives, solvation structure, complexation interactions

1 Introduction

As a pivotal component of new-energy systems, rechargeable batteries have undergone remarkable advancements in recent years [1–3]. Among the available battery systems, aqueous zinc-ion batteries (AZIBs) have emerged as promising competitive candidates in large-scale energy storage due to their cost-effectiveness, inherent safety, and high crustal abundance and theoretical capacity (820 mAh g^{-1}) of zinc (Zn) anode [4–6]. According to cathode reaction mechanisms, AZIBs can be categorized into two types: ion de/intercalation and conversion reaction types [7–9]. With regard to ion de/intercalation-type AZIBs, the charge/discharge processes are accomplished through individual Zn^{2+}/H^+ ion insertion/extraction or their co-de/intercalation into the cathode, most of which are based on single-electron redox mechanisms with relatively low voltages and capacities [10]. Moreover, the repeated ion de/intercalation process can readily induce cathode structural change, causing its structure to collapse or dissolution [11]. This would significantly restrict the cycle stability of batteries. In contrast, AZIBs based on conversion reaction mechanisms exhibit distinctive multi-electron redox processes during operation, endowing them with enhanced specific capacity and elevated operating voltage [12–15].

As a typical conversion-type AZIBs, aqueous zinc-iodine (Zn–I_2) batteries have garnered extensive attention owing to their abundant reserves, low cost, and promising long-term cycling stability of iodine (I_2) [16–18]. Nevertheless, conventional aqueous Zn–I_2 batteries rely on the iodine/iodide (I_2/I^-) redox chemistry, constrained by low operating voltage (~1.3 V) and moderate theoretical capacity (211 mAh g^{-1}), consequently failing to meet large-scale energy storage demands. To this end, the research focus has moved to the four-electron conversion-type aqueous Zn–I_2 batteries, achieved by iodine cation/iodine/iodide (I^+/I_2/I^-) redox reactions [19, 20]. However, the practical implementation of such systems faces critical challenges: I^+ ions exhibit intrinsic instability in aqueous media due to their high susceptibility to hydrolysis, coupled with barriers in electrochemical activation from I_2.

Most reported strategies employ $ZnCl_2$-based electrolytes or chloride-containing (Cl^-) additives to stabilize I^+, leveraging the interaction between nucleophilic Cl^- and electrophilic I^+ to form iodine monochloride (ICl) intermediates to suppress I^+ hydrolysis [21, 22]. Unfortunately, low-concentration $ZnCl_2$ electrolytes or Cl^--containing additives fail to fully stabilize I^+ due to the

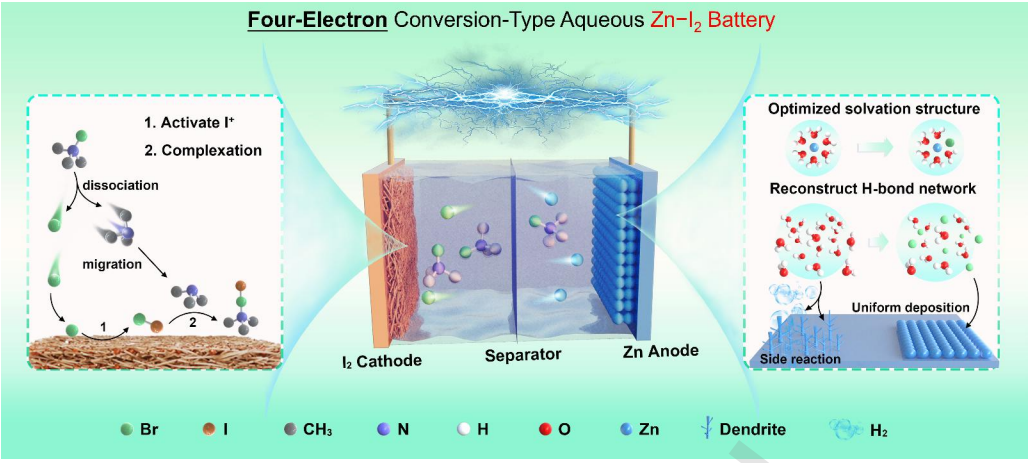

Figure 1. Schematic diagram of the TMBr enabled four-electron conversion-type aqueous Zn–I_2 batteries, including the dual-side shielding mechanism of electrolyte regulation.

high activity of H_2O molecules in aqueous electrolytes. To mitigate this issue, highly concentrated $ZnCl_2$-based electrolytes (e.g., 19 m $ZnCl_2$ + 19 m LiCl + 8 m CH_3CN system [23]) have been proposed to inhibit free H_2O activity to stabilize I^+. The accompanying drawbacks are obvious, such as high production costs and relatively low ionic conductivity of electrolytes. Moreover, the strong chemical corrosion of Cl^- toward the Zn anode and other battery components (like stainless steel battery case) reduces the lifespan of batteries. Apart from the problems of the I_2 cathode, the high reactivity of H_2O molecules and the heterogeneous electric field distribution make Zn anodes inherently suffer from hydrogen evolution side reactions (HER) and Zn dendrite growth [24–26], restricting the stability of Zn anodes. These challenges make it highly necessary to develop an effective strategy that could play dual-side shielding roles on the cathode and anode to bring four-electron aqueous Zn–I_2 batteries one step closer to being a viable technology.

Herein, we have selected 2 M $ZnSO_4$ (ZSO) as a zinc salt solution to avoid the existence of Cl^- induced chemical corrosion on the Zn anode, while introducing 0.5 M trimethylammonium bromide (C_3H_9N·HBr, TMBr) additive to stabilize the Zn anode and I^+ generated during high-voltage reactions, constituting a "Dual-Side Shielding" strategy (Fig. 1). On the one hand, bromide ions (Br^-) could participate in the solvation structure of the electrolyte due to their strong coordination capability with Zn^{2+}. Concurrently, Br^- ions could also disrupt and reconstruct the original hydrogen-bond (H-bond) network by substituting H_2O–H_2O interactions with Br^-–H_2O coordination, reducing the content of active H_2O molecules in the electrolyte system. This effectively alleviates HER and enhances Zn anode stability, making Zn||Zn symmetric cells achieve a cycling lifespan of 600 h under 5 mA cm^{-2} and 5 mAh cm^{-2}, and enabling Zn||Cu cells to realize an average Coulombic efficiency (CE) of 99.7%. On the other hand, the Br^- could activate I_2 to form I^+ via the formation of intermediate IBr species. And the trimethylammonium cations ($C_3H_{10}N^+$, TM^+) could further stabilize I^+ through the unique complexation capability of ammonium salts. The synergistic effects from the anion and cation of TMBr successfully activate and stabilize a four-electron I_2-involved reaction process, enabling Zn–I_2 batteries deliver a high specific capacity of 250 mAh g^{-1} at 3 A g^{-1} with 15,000 cycles (cycling time >2,400 h). The assembled pouch cell achieves a practical capacity of 160 mAh at 0.2 A g^{-1}, corresponding to an energy density of 367.4 Wh kg^{-1} (based on I_2 mass). Additional, owing to the particular H-bond network disruption capability of TMBr, the designed electrolyte also endows the batteries with superior low-temperature performance at –10 °C: Zn||Zn symmetric cells with a steady cycling lifetime over 1000 h and Zn–I_2 battery with capacities >200 mAh g^{-1} for more than 4,400 cycles.

2 Experimental

2.1 Preparation of electrolytes

The 2 M $ZnSO_4$ (ZSO) electrolyte was prepared by mixing $ZnSO_4$·$7H_2O$ and deionized water (DIW) in a 250 mL blue cap bottle. Different concentrations of TMBr-based electrolytes were prepared by adding corresponding amount (1.5 mmol, 2.5 mmol, and 3.5 mmol, respectively) of TMBr into 5 mL ZSO electrolyte.

2.2 Synthesis of I_2 cathode

Firstly, self-supporting carbon nanotube cathodes (SSCC) were synthesized. 0.035 g CNT was added to a 48 mL custom sealed reaction bottle, followed by the addition of 30 mL DIW and 10 mL 0.1 M HCl. The mixture was ultrasonicated for 3 h. After this, 5 mg KB was introduced into the solution and thoroughly mixed. The mixture was subjected to filtration for self-assembly and washed multiple times with 0.1 M HCl, DIW, and ethanol. Finally, the product was dried in a 70 °C drying oven to obtain SSCC. To synthesize I_2 cathode, SSCC and I_2 powder were weighed according to a weight ratio of 3: 1 and put them into 250 mL blue-cap bottle at 80 °C for 6 h (I_2 loading mass: ~30 wt%). The resulting product was SSCC/I_2. Subsequently, the SSCC/I_2 was cut into 10 mm diameter cathode sheets with I_2 loading of ~2 mg cm^{-2}.

3 Results and discussion

3.1 Characterizations on the fundamental properties of electrolytes

Considering halogen elements can form interhalogen

compounds and Cl^- has the corrosion risk to battery components, Br^- ions with the ability to form another stable interhalogen compound IBr containing I^+ other than ICl would

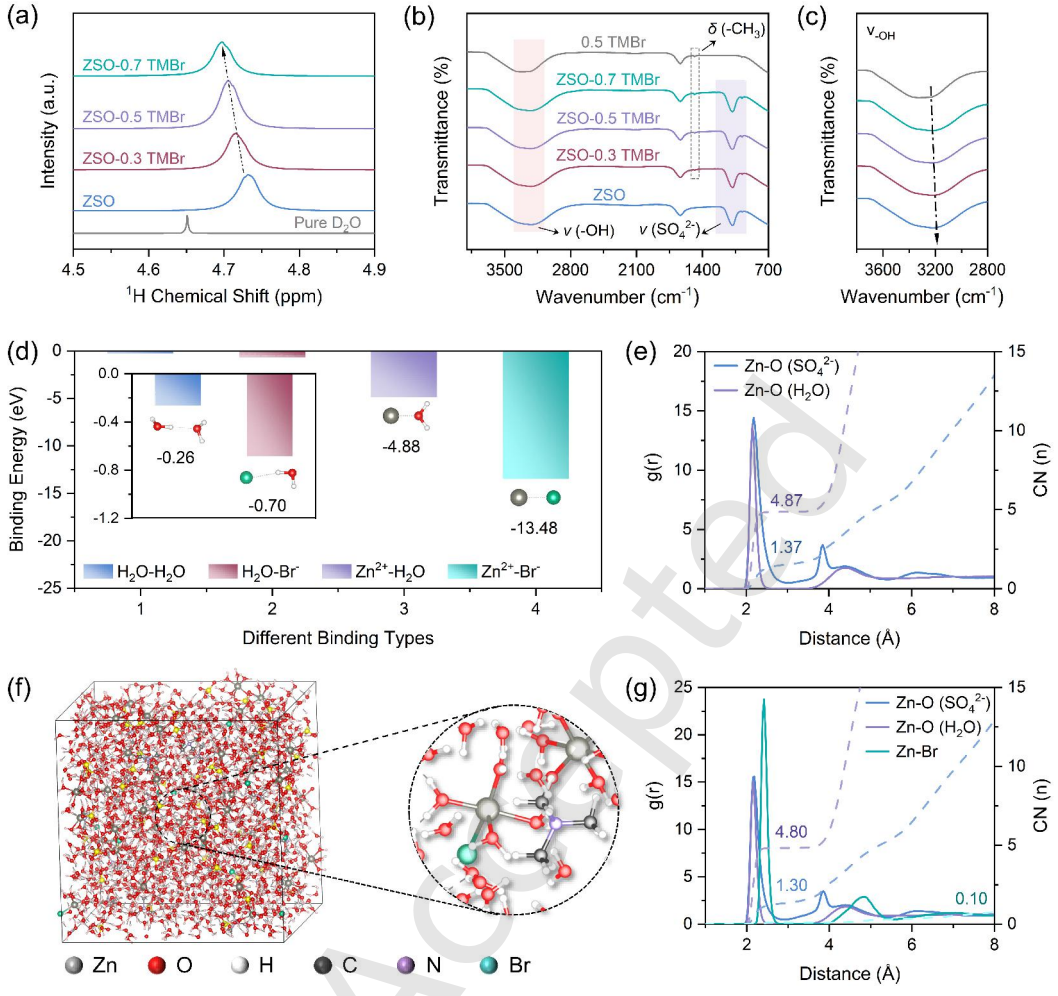

Figure 2. Characterizations on the fundamental properties of ZSO electrolytes containing different concentrations of TMBr. (a) ^1H NMR spectra. (b) FTIR full spectra and (c) zoom-in view around the –OH region. (d) Binding energy of H_2O–H_2O, H_2O–Br^-, Zn^{2+}–H_2O, and Zn^{2+}–Br^-. The g(r) and CN of Zn–O and Zn–Br in the (e) ZSO and (g) ZSO-TMBr electrolytes. (f) MD models of the ZSO-TMBr electrolyte and magnified TMBr molecular (H: white, O: red, Zn: ash black, Br: bright green).

be good additive anion component to motivate the four-electron conversion of I_2. Meanwhile, Br^- ions also have the ability to optimize the Zn^{2+} solvation structure and regulate the Zn deposition process, bringing function to prevent the anode corrosion [27]. Besides activating I_2 to I^+, the stabilization of I^+ to avoid hydrolysis is of great importance for the long-term operation of four-electron aqueous Zn–I_2 batteries. Ammonium salt cations bring hope to this challenge because they have coordination capability with I^+ and Br^- to form stable compound [28]. In this circumstance, TMBr has been rationally selected as the electrolyte additive to play dual-side shielding roles on the cathode and anode to boosting the performance of Zn–I_2 batteries, as it can provide both Br^- and ammonium salt cation (TM^+).

To investigate the effectiveness of the selected electrolyte additive, the fundamental properties of ZSO electrolytes containing different concentrations (x M, x = 0.3, 0.5, 0.7) of TMBr was characterized, designated as ZSO-0.3 TMBr, ZSO-0.5 TMBr, and ZSO-0.7 TMBr, respectively. The electrolyte structure was first studied by using hydrogen nuclear magnetic resonance (^1H NMR) spectra. As shown in Fig. 2(a), compared with D_2O, the chemical shift of ZSO shifts from 4.65 ppm to 4.74 ppm, which is attributed to the coordination between Zn^{2+} and H_2O molecules that results in reduced shielding effects and a downfield shift [29]. However, the ^1H chemical shift exhibits an upfield displacement with the increase of TMBr concentration. This might be ascribed to the following factors: 1) Br^- partially participates in the Zn^{2+} solvation structure that reduces the number of directly coordinated water molecules around Zn^{2+}, diminishing the de-shielding effect; 2) Br^- disrupts the H-bond network of H_2O and releases free H_2O molecules, rendering the proton signal shifting toward pure D_2O. Fourier transform infrared (FTIR) and Raman spectra were subsequently employed to validate this speculation. As depicted in Fig. 2(b), besides the characteristic peaks of H_2O at 3200 ~ 3600 cm^{-1} and 1640 cm^{-1}, the peaks at 1079.4 cm^{-1} and 1459.8 cm^{-1} corresponding to the stretching vibration of SO_4^{2-} and bending vibration of $-CH_3$ emerge. Notably, the –OH peak position shifts from 3218.6 cm^{-1} to 3224.4 cm^{-1} with increasing TMBr concentration (Fig. 2(c)), indicating the H-bond network of H_2O–H_2O is disrupted by the enhanced bond energy of –OH [30]. Additionally, the –OH characteristic peak exhibits a blue shift in Raman spectra

(Fig. S1 in the ESM), providing further corroboration for the break of H-bond network. By fitting the Raman peak of the –OH groups, three Gaussian peaks assigned to the strong, medium, and weak H-bonds can be identified at 3220, 3420, and 3600 cm^{-1} (Fig. S2

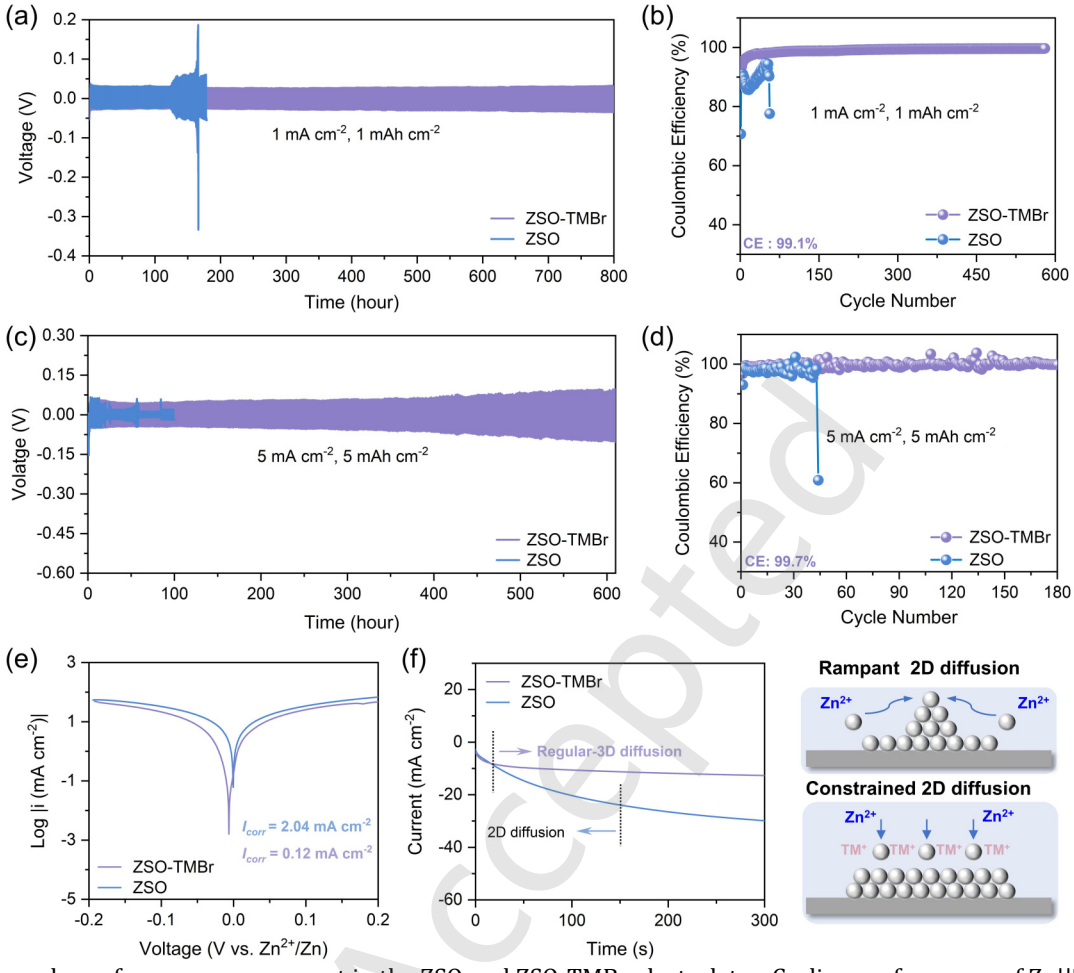

Figure 3. Zn anode performance assessment in the ZSO and ZSO-TMBr electrolytes. Cycling performance of Zn||Zn symmetrical cells at (a) 1 mA cm^{-2} for 1 mAh cm^{-2} and (c) 5 mA cm^{-2} for 5 mAh cm^{-2}. CE plots of Zn||Cu cells at (b) 1 mA cm^{-2} for 1 mAh cm^{-2} and (d) 5 mA cm^{-2} for 5 mAh cm^{-2}. (e) Tafel plots of electrochemistry corrosion at 10 mV min^{-1}. (f) I–t profiles of Zn||Zn symmetric cells at –150 mV and corresponding schematic diagram of Zn^{2+} diffusion path.

in the ESM), respectively [31]. As described in Fig. S3, the content of strong H-bond decreases while the weak H-bond initially increases and subsequently declines with progressive concentration increment of TMBr, suggesting the breakage and reconstruction of the H-bond network.

Theoretical calculations were then conducted to further study the electrolyte structure with/without TMBr. Higher binding energies are revealed in Br^-–H_2O (–0.70 eV) and Zn^{2+}–Br^- (–13.48 eV) interactions (Fig. 2(d)), compared with those in H_2O–H_2O (–0.26 eV) and Zn^{2+}–H_2O (–4.88 eV), manifesting that Br^- can indeed participate in the Zn^{2+} solvation structure and rebuild the H-bond network. The decrease in H-bond number of H_2O–H_2O and increase in H-bond number of H_2O–Br^- further corroborate this conclusion (Tables S1 and S2 in the ESM). Following this, relevant molecular dynamics (MD) simulations were executed (Fig. 2(f) and Figs. S4 and S5 in the ESM) to get the coordination numbers (CNs) of Zn–O and Zn–Br through the radial distribution function (RDF, g(r)). Computational results (Figs. 2(e) and 2(g)) disclose that the CN of Zn–O (H_2O) decreases from 4.87 to 4.80, while a new Zn–Br coordination with a CN of 0.1 emerges upon TMBr addition. These results collectively demonstrate that TMBr could optimize the solvation structure and disrupt the H-bond network, thereby contributing to facilitating controlled Zn deposition and hampering free H_2O activity. To ensure fully exert the regulatory effect of TMBr and maintain a high ionic conductivity (Fig. S6 in the ESM) of electrolyte systems, 0.5 M TMBr was selected as the optimal additive concentration. Therefore, the optimized electrolyte system (ZSO-0.5 TMBr) was employed in subsequent studies, referred to as ZSO-TMBr.

3.2 Evaluation of anode stability

After verifying the beneficial function brought to the electrolyte itself, the stabilizing effect of ZSO-TMBr on the Zn anode was comprehensively evaluated by electrochemical tests. Since the performance of Zn||Zn symmetric cells could serve as a critical indicator for assessing Zn anode stability, their long-term cycling performance was checked. As shown in Fig. 3(a) and Fig. S7, under the condition of 1 mA cm^{-2} and 1 mAh cm^{-2}, the Zn||Zn symmetric cell employing the ZSO-TMBr electrolyte demonstrates stable cycling for lasting 800 h operation, surpassing the 150 h in the ZSO electrolyte. This performance enhancement confirms the ability of ZSO-

TMBr in restraining side reactions involving HER and dendritic Zn growth. Notably, the relative higher deposition/dissolution overpotential in ZSO-TMBr (66.6 mV) than that in ZSO (57.8 mV) favors a uniform and compact Zn deposition tendency (Fig. S8 in the ESM) [27]. To further

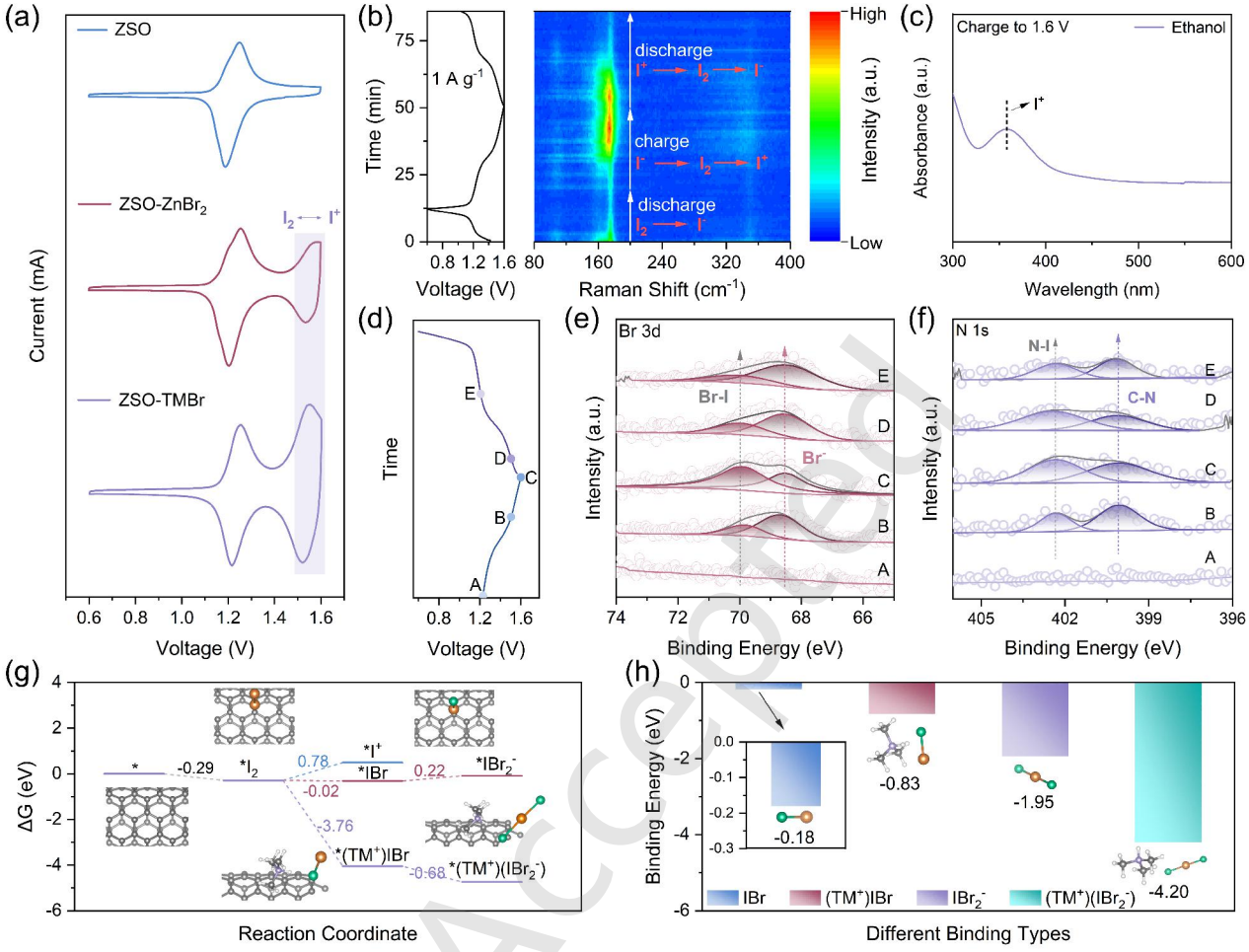

Figure 4. Characterizations of ZSO-TMBr electrolyte towards I^+. (a) CV curves of Zn–I_2 batteries with ZSO, ZSO-$ZnBr_2$, and ZSO-TMBr electrolytes. (b) In situ Raman spectra of Zn–I_2 batteries with ZSO-TMBr electrolyte. (c) UV–vis spectra of cathodes charged to 1.6 V immersed in ethanol solution. (d) Ex situ XPS spectra of (e) Br 3s and (f) N 1s for cathodes at different charge-discharge states (A: pristine cathode, B: charge to 1.5 V, C: charge to 1.6 V, D: discharge to 1.5 V, E: discharge to 1.2 V). (g) Gibbs free energy change (ΔG) for forming different I species. (h) Binding energy of different I species towards I^+. (H: white, C: black, Br: bright green, N: purple, I: orange).

validate the TMBr rendered high reversibility of Zn plating/stripping, Zn||Cu asymmetric cells were also tested under identical conditions. The cell using ZSO-TMBr exhibits over 580 cycles with an average Coulombic efficiency (CE) of 99.1%, significantly outperforming the ZSO-based cell (Fig. 3(b)). Analysis of the corresponding charge-discharge profiles (Fig. S9 in the ESM) reveals that the CE of ZSO-TMBr-based Zn||Cu cell exceeds 99% after 50 cycles, whereas the ZSO-based cell fails after 100 cycle due to rapid capacity decay during the stripping process. To assess the high-rate stability of Zn anode, the electrochemical test was then conducted at 5 mA cm^{-2} and 5 mAh cm^{-2}. As depicted in Figs. 3(c) and 3(d), the ZSO-TMBr electrolyte enables the symmetric cell to sustain stable operation for over 600 h and the Zn||Cu cell to achieve 180 cycles with a CE of 99.7%, much superior to the ZSO electrolyte (Fig. S10 in the ESM). These results collectively indicate the markedly improved stability of Zn anode in the ZSO-TMBr electrolyte, which can be attributed to the Br^--mediated modulation of the electrolyte solvation structure and reorganization of the H-bond network.

Additional electrochemical measurements were further implemented to corroborate the constraint of HER and Zn dendrite formation. Linear sweep voltammetry (LSV, Fig. S11 in the ESM) discloses lower HER onset potential and corrosion current in the ZSO-TMBr electrolyte. Similarly, the ZSO-TMBr-based Tafel plot just delivers a corrosion current of 0.12 mA cm^{-2}, much lower than the 2.04 mA cm^{-2} in ZSO (Fig. 3(e)), indicating the ZSO-TMBr can effectively restrain the electrochemical corrosion of Zn [32, 33]. It can be seen from the X-ray powder diffraction (XRD) patterns (Fig. S12 in the ESM), zinc hydroxide sulfate ($Zn_4SO_4(OH)_6{\cdot}4H_2O$, ZHS) located at 8.5° appears in the ZSO and is absent in the ZSO-TMBr, certifying the parasitic reactions can be mitigated by TMBr. Moreover, the morphology of Zn anodes after 50 cycles was characterized by scanning electron microscope (SEM) (Fig. S13 in the ESM). Compared with the Zn cycled in the ZSO electrolyte, Zn growth is more regular and denser in

the ZSO-TMBr electrolyte, effectively mitigating dendrite formation.

To explore the inhibition mechanism of side reactions by TMBr, the reaction kinetics of the Zn anode were analyzed. As illustrated in Fig. S14, the ZSO-TMBr possesses a larger Zn^{2+} transference number (0.51) than ZSO (0.38), which could facilitate homogeneous Zn^{2+} transport to uniform the Zn^{2+} ion flux around the anode surface. The Zn deposition mechanism was then probed via chronoamperometry (I–t curves, Fig. 3(f)). It is clear that the ZSO-TMBr achieves a shorter two-dimensional (2D) diffusion (25 s) and a stable three-dimensional (3D) diffusion process, manifesting uniform nucleation and growth manner during the Zn deposition process [34, 35]. Therefore, the ZSO-TMBr electrolyte, optimized by the multifunctional TMBr additive, stabilizes the Zn anode with suppressed side reactions and dendrite growth.

3.3 Evaluation of I_2 cathode stability

Although the benefits brought to the electrolyte and Zn anode by ZSO-TMBr, constructing stable four-electron-transfer Zn–I_2 batteries still requires addressing the stability issues of I^+ at the cathode side. To this end, the function mechanism of TMBr on I^+ was investigated. As shown in Fig. 4(a), compared with the ZSO-based battery, a pair of high-voltage redox peaks near 1.5 V appear in the batteries with ZSO-$ZnBr_2$ and ZSO-TMBr electrolytes, which may correspond to either I_2/I^+ or Br^-/Br_2 redox couples. Given that the Br^-/Br_2 redox peaks typically reside between 1.6 and 1.8 V [36, 37], the observed high-voltage redox process is more likely attributed to the I_2/I^+ redox pair. Since a more pronounced high-voltage redox process occurs in the ZSO-TMBr electrolyte, we speculate that Br^- could activate and stabilize I^+, while TM^+ could further stabilize I^+ by complexation interaction. In situ Raman spectra of the I_2 cathode (Fig. 4(b)) during discharge/charge process were employed to confirm the I_2/I^+ conversion process. During the 1st discharge process, the intensity reduction of the I_2 signal at 175 cm^{-1} indicates the conversion reaction from I_2 to I^-. However, in the following charge process, the intensity of the I_2 signal experiences a first increase and then decrease phenomenon, suggesting further I_2 transformation to I^+ after I^--to-I_2 conversion. In the subsequent discharge cycle, the reverse I_2 signal variation in the high-voltage reaction region illustrates the high reversibility of the I_2/I^+ process. It should be mentioned that no Br_2 specie signals [38] (Br_2: 251 cm^{-1} and 290 cm^{-1}) have been detected, validating the exclusive involvement of I_2/I^+ conversion. Due to the close peak position of I^+ (172 cm^{-1}) to that of I_2 (175 cm^{-1}), no evident I^+ signal has been detected [39]. In this case, ultraviolet-visible (UV–vis) spectra were collected to directly verify the existence of I^+ (Fig. 4(c)). When immersing the charged cathode in ethanol, a distinct absorption peak corresponding to I^+ emerges at 350 nm, which can be attributed to the ease solution of I^+ in organic solvents [40]. This demonstrates that I^+ exists in cathode via electrolyte stabilization, and the high-voltage I_2/I^+ conversion process indeed occurs. However, the detailed stabilization mechanism of I^+ by TMBr requires deeper investigation.

Considering the widespread use of bromide-containing ammonium salts as complexing agents for stabilizing the Br_2 cathode in aqueous Zn-Br_2 batteries, we speculate that I^+ can also be stabilized by the complexation interaction with the TMBr additive owing to the analogous chemical properties among polyhalides [41]. To certify the viewpoint, dissolution test of IBr in ZSO and various Br^--containing ammonium salts was studied (Figs. S15a–S15d in the ESM). As displayed in Fig. S15e, from left to right are ZSO, TMBr, tetraethylammonium bromide (TEBr), 1-ethyl-1-methylpyrrolidinium bromide (PBr), and tetrabutylammonium bromide (TBBr) solutions, respectively. Compared with ZSO, the color becomes light for TMBr solution. From TEBr to TBBr, the color of the solutions gradually fades accompanied by precipitate formation, and longer cation chain lengths result in obvious turbidity substances and darker precipitates. Therefore, TMBr and other ammonium salt solutions will respectively form liquid complexes and precipitate complexes with I^+, and the complexation strength can be intensified by increasing the chain length. Theoretically, strong complexation should enhance I^+ stability, leading to improved battery performance. However, when a Zn–I_2 battery employing ZSO-PBr electrolyte has been tested (Fig. S16 in the ESM), continuous capacity decay occurs at 5 A g^{-1} until the cell fails completely. The analysis of the disassembled cathode (inset of Fig. S16 in the ESM) reveals the precipitate complexes formed by 1-ethyl-1-methylpyrrolidinium cation (P^+), Br^- and I^+ fully cover the cathode surface and irreversibly consume I_2 active material, leading to rapid cell degradation. Therefore, excessive complexation action proves detrimental to the performance of four-electron conversion-type Zn–I_2 batteries. In contrast, TMBr's moderate complexation strength can not only stabilize I^+ but also ensure the reversibility of I^+ conversion by means of avoiding active material consumption arisen from precipitate formation, contributing to enabling stable four-electron conversion. The UV–vis spectra of IBr dissolved in H_2O, ZSO, and ZSO-TMBr were applied to further validate the complexation capability of TMBr (Fig. S17 in the ESM). Even after dissolving 4 h, stable retention of I^+ can still be observed in ZSO-TMBr, whereas significant hydrolysis of I^+ to I_2 occurs in H_2O and ZSO. The high stability of I^+ in ZSO-TMBr is attributed to the complexation effect of TM^+ and Br^- on I^+.

The beneficial effects of ZSO-TMBr brought to the I_2 cathode were further corroborated by ex situ XPS analysis and theoretical calculations. Fig. 4(d) presents the charge-discharge profiles of a Zn–I_2 battery employing ZSO-TMBr electrolyte. Five distinct states were selected to probe the I^+ conversion mechanism: pristine state (A), charged to 1.5 V (B), charged to 1.6 V (C), discharged to 1.5 V (D), and discharged to 1.2 V (E). The corresponding ex situ high-resolution XPS spectra of I 3d, N 1s, and Br 3d are shown in Fig. S18, and Figs. 4(e) and 4(f), respectively. As portrayed in Fig. S18a, the I 3d binding energy increases progressively from state A (630.8 eV, 619.4 eV) to C (631.3 eV, 620.0 eV) and reverts to its initial value from C to E (630.9 eV, 619.4 eV), confirming the reversible conversion between I^0 and I^+ and the high reversibility of I_2/I^+ redox couple. In Br 3d spectra (Fig. 4(e)), the intensity of the Br–I bond at 70 eV first increases (A to C) and subsequently decreases (C to E), and a parallel trend is observed for the N–I bond at 402.8 eV in the N 1s spectra [42] (Fig. 4(f); Fig. S18b in the ESM). These synchronized variations indicate that Br^- could

activate I^+, while TM^+ further stabilizes it through complexation action of TM^+, Br^- and I^+. The homogeneous distribution of N, I, and Br elements on the cycled cathode provides additional support for this mechanism (Fig. S19 in the ESM). Gibbs free energy change (ΔG) was then calculated (Fig. 4(g)), and it elucidates that Br^- enables spontaneous IBr formation from I_2, lowering the energy barrier for I^+ generation and testifying that Br^- can serve as the activator of I^+. In the concurrent presence of Br^- and TM^+, the energy barrier for I_2-to-I^+ conversion is further reduced by the formation of $(TM^+)IBr$ and $(TM^+)(IBr_2^-)$ complexes. Additionally, compared with IBr and IBr_2^-, more negative binding energy is found in $(TM^+)IBr$ and $(TM^+)(IBr_2^-)$

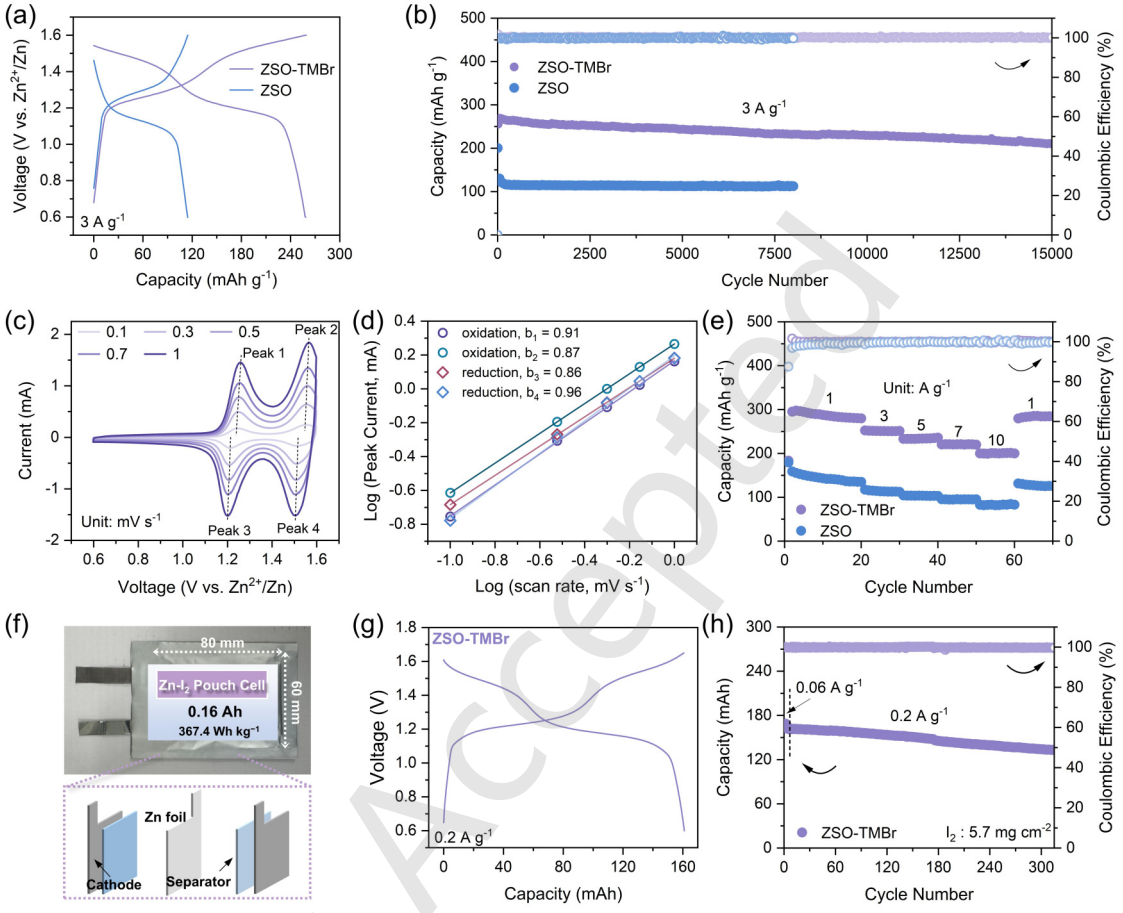

Figure 5. Electrochemistry performance of Zn–I_2 batteries. (a) Charge-discharge curves and (b) cycling performance at 3 A g^{-1} with ZSO and ZSO-TMBr electrolytes. (c) CV curves at different scan rates. (d) Dependence correlation plots of the test current on scan rate at corresponding peak potentials. (e) Rate performance. (f) Optical photo of Zn–I_2 pouch cell and corresponding internal configuration. (g) Charge-discharge curves and (h) cycling performance of the pouch cell at 0.2 A g^{-1}

complexes (Fig. 4(h)). Also, the binding force of TMBr toward I^+ is stronger than that of Cl^- applied in most reports (Fig. S20 in the ESM). Consequently, the synergistic interplay of TMBr activation and complexation functions collectively facilitate the realization of reversible four-electron conversion-type Zn–I_2 batteries.

3.4 Room-temperature performance of Zn–I_2 batteries

As demonstrated above, the introduction of TMBr as the electrolyte additive could simultaneously address stability issues at both the Zn anode and I_2 cathode. To validate the feasibility of this dual-side shielding function, comprehensive electrochemical evaluations were conducted on Zn–I_2 full batteries. The charge-discharge profiles (Fig. 5(a)) reveal a distinct 1.5 V plateau and doubled capacity in the ZSO-TMBr electrolyte compared to ZSO, primarily attributing to the stabilized four-electron conversion process involving $I^-/I_2/I^+$ redox couples. As shown in Fig. 5(b), the ZSO-TMBr-based Zn–I_2 battery delivers an initial capacity of 250 mAh g^{-1} and could maintain 15,000 stable cycles (time >2,400 h) at 3 A g^{-1}, outperforming the performance reported in recent studies (Table S3 in the ESM). Additionally, the battery could still achieve a capacity of 213 mAh g^{-1} with a capacity retention of 85% over 20,000 cycles at 5 A g^{-1} (Fig. S21 in the ESM). It should be mentioned that no obvious corrosion pits appear on the Zn anodes after both short-term (100 cycles) and long-term (1000 cycles) cycling (Fig. S22 in the ESM). This once again proves the effectiveness of the designed dual-side shielding electrolyte.

After confirming the improved reversible capacity and lifetime of ZSO-TMBr-based Zn–I_2 batteries, their reaction kinetics were investigated through cyclic voltammetry (CV) curves at different scan rates. Favorable reaction kinetics can be reflected by Fig. 5(c), because there is no obvious change in polarization by increasing the scan rate from 0.1 to 1 mV s^{-1}. Calculated from the relationship $i = av^b$, the oxidation/reduction peaks (labeled Peak 1–4) exhibit b-values of 0.91, 0.87, 0.86, and 0.96, respectively (Fig. 5(d)).

These b-values close to 1 indicate a surface-controlled, capacitive-dominated process, and the capacitive contribution ratios are 73.68%, 80.25%, 83.03%, 84.99%, and 90.53% at 0.1, 0.3, 0.5, 0.7, and 1 mV s^{-1} (Fig. S23 in the ESM), confirming the faster reaction kinetics of I_2 species [43–45]. Consequently, the Zn–I_2 battery certifies great rate capability: capacities of 300, 250, 221, 210, and 200 mAh g^{-1} at 1, 3, 5, 7, and 10 A g^{-1}, and the capacity could recover to 290 mAh g^{-1} as the current returns to 1 A g^{-1} (Fig. 5(e)). Furthermore, on account of the four-electron conversion mechanism, a constant twice capacity can be maintained for Zn–I_2 batteries in ZSO-TMBr electrolyte compared to the ZSO electrolyte. To demonstrate the effectiveness of the designed electrolyte in practical applications, a ZSO-TMBr-based pouch

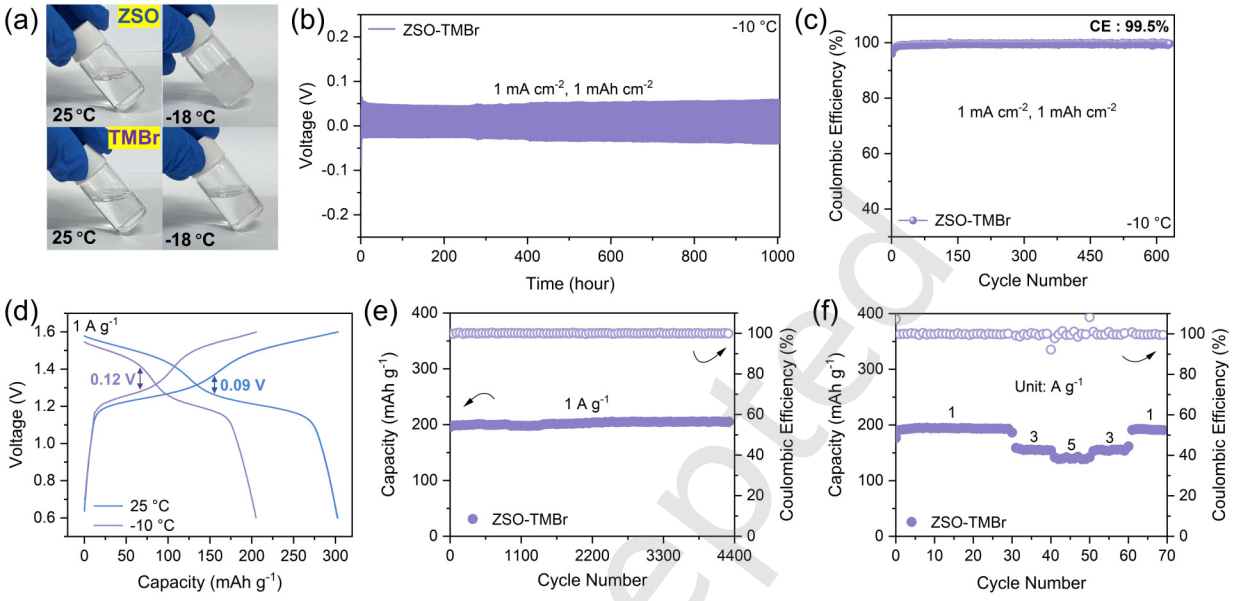

Figure 6. Low-temperature performance evaluation of ZSO-TMBr electrolyte. (a) Optical photos of ZSO and ZSO-TMBr electrolytes at −18 °C for 2 h. (b) Cycling performance of Zn||Zn symmetrical cells and (c) CE plots of Zn||Cu cells at 1 mA cm^{-2}, 1 mAh cm^{-2}, and −10 °C. (d) Charge-discharge curves and (e) cycling performance of Zn–I_2 batteries at −10 °C. (f) Rate capability of Zn–I_2 batteries at 1 A g^{-1}.

cell (6 × 8 cm^2) was fabricated, featuring a loading mass of 5.73 mg cm^{-2} based on I_2 (total I_2 mass: 550 mg) (Fig. 5(f) and Fig. S24 in the ESM). The discharge profile retains a prominent 1.5 V plateau despite scaled-up dimensions (Fig. 5(g)). At 0.2 A g^{-1}, the cell delivers 160 mAh capacity with 83.7% capacity retention after 300 cycles, achieving an energy density of 367.4 Wh kg^{-1} based on the I_2 active material (Fig. 5(h); Fig. S25 in the ESM). These results suggest the practical viability of this dual-side shielding strategy in large-format devices.

3.5 Low-temperature performance of Zn–I_2 batteries

Since TMBr disrupts the H-bond network of the electrolyte, it can lower the electrolyte's freezing point, promising to help Zn–I_2 batteries operate under low-temperature conditions [46]. As shown in Fig. 6(a), both ZSO and ZSO-TMBr electrolytes display excellent fluidity at room temperature (25 °C). However, after being maintained at −18 °C for 2 h, ZSO undergoes solidification, whereas ZSO-TMBr retains liquid-state fluidity, stating its potential for realizing low-temperature Zn–I_2 batteries. Therefore, electrochemistry performance measurements of batteries with ZSO-TMBr were performed at −10 °C. It can be seen from Fig. 6(b) and Fig. S26 in the ESM that the Zn||Zn symmetric cells achieve stable cycling over 1000 h at 1 mA cm^{-2} for 1 mAh cm^{-2} and 1,400 h at 0.5 mA cm^{-2} for 0.5 mAh cm^{-2}. At the condition of 1 mA cm^{-2} for 1 mAh cm^{-2}, the Zn||Cu cell maintains over 600 cycles with an average CE of 99.5% (Fig. 6(c)), accompanied by low polarization and reversible Zn deposition/stripping in their voltage profiles (Fig. S27 in the ESM). These results confirm that the ZSO-TMBr electrolyte delivers certain low-temperature stability and a role in hindering anode side reactions. When moving to Zn–I_2 full cells, discharge plateaus of 1.5 V and 1.2 V ascribed to the four-electron conversion mechanism remain well (Fig. 6(d)), and the polarization in galvanostatic profiles experiences no obvious increase. Besides, the cell could deliver a stable capacity around 200 mAh g^{-1} at 1 A g^{-1} over 4,400 cycles without capacity attenuation (Fig. 6(e)). Importantly, the cell also possesses superior rate capability with specific capacities of 200, 165, and 148 mAh g^{-1} at 1, 3, and 5 A g^{-1} (Fig. 6(f)), respectively, implying the fast ion transport ability of the designed electrolyte at −10 °C. Even at −15 °C, the Zn||Zn symmetric cell sustains 640 h of cycling at 0.5 mA cm^{-2} for 0.5 mAh cm^{-2}, and the Zn–I_2 full battery exhibits an initial capacity of 150 mAh g^{-1} with 250 cycles at 1 A g^{-1} (Fig. S28 in the ESM). Therefore, the dual-side shielding function of ZSO-TMBr can be well maintained at low-temperature conditions, make the Zn–I_2 batteries retain four-electron redox chemistry and stable cycling, and also adapt to cryogenic environments.

4 Conclusions

In summary, the TMBr additive with a dual-side shielding function has been introduced into the electrolyte to simultaneously stabilize the Zn anode and I_2 cathode. From

the anode perspective, Br^- ions could participate in the solvation structure of the electrolyte and reconstruct the H-bond network, which facilitates the desolvation process of Zn^{2+} and reduces the activity of free H_2O molecules. This synergistic effect enables uniform Zn deposition and effectively restrains HER. For the cathode side, TMBr can activate and stabilize of I+ by forming stable intermediate products ($(TM^+)IBr$ and $(TM^+)(IBr_2^-)$) through complexation interactions, efficiently stabilizing high-voltage I_2/I^+ conversion process. Consequently, high-performance four-electron conversion-type $Zn–I_2$ batteries have been successfully constructed: an initial capacity of 250 mAh g^{-1} over 15,000 cycles at 3 A g^{-1} and an energy density of 367.4 Wh kg^{-1} with a lifetime exceeding 300 cycles. Additionally, the unique H-bond disrupting capability of TMBr also makes the ZSO-TMBr electrolyte possess low-temperature tolerance. Consequently, at −10 °C, the Zn||Zn symmetric cell exhibits cycling stability exceeding 1000 h, and the $Zn–I_2$ full cell delivers a capacity around 200 mAh g^{-1} over 4,400 cycles at 1 A g^{-1}. This work provides new insights into the research of four-electron aqueous $Zn–I_2$ batteries, promising to advance the development of AZIBs energy storage systems.

Electronic Supplementary Material: Supplementary material (please provide the brief detail of the ESM) is available in the online version of this article at https://doi.org/10.26599/NR.2026.94908914.

Data availability

All data needed to support the conclusions in the paper are presented in the manuscript and/or the Electronic Supplementary Material. Additional data related to this paper may be requested from the corresponding author upon request.

Acknowledgements

This work was supported by the National Natural Science Foundation of China (Grant 92372206), Jilin Province Science and Technology Development Plan Funding Project (Grant YDZJ202301ZYTS545), and National Natural Science Foundation of China Excellent Young Scientists.

Declaration of competing interest

All the contributing authors report no conflict of interests in this work.

Author contribution statement

Z. B. Z.: Data curation, validation, writing manuscript, experimental design. J. G. and C. L. C.: experimental validation. X. B. Z., and G. H.: Project administration, supervision, funding acquisition, manuscript correcting. J. M. Y: manuscript correcting. All the authors have approved the final manuscript.

Informed consent

Not applicable

Ethics statement

Not applicable

Use of AI statement

None.

References

[1] Goodenough, J. B.; Kim, Y. Challenges for Rechargeable Li Batteries. *Chem. Mater*. **2009**, *22*, 587–603.

[2] Bruce, P. G.; Freunberger, S. A.; Hardwick, L. J.; Tarascon, J. M. Li–O_2 and Li–S batteries with high energy storage. *Nat. Mater.* **2011**, *11*, 19–29.

[3] Adenusi, H.; Chass, G. A.; Passerini, S.; Tian, K. V.; Chen, G. Lithium Batteries and the Solid Electrolyte Interphase (SEI)—Progress and Outlook. *Adv. Energy Mater*. **2023**, *13*, 2203307.

[4] Liu, X.; Han, Q.; Ma, Q.; Wang, Y.; Liu, C. Cellulose-Acetate Coating by Integrating Ester Group with Zinc Salt for Dendrite-Free Zn Metal Anodes. *Small* **2022**, *18*, e2203327.

[5] Qian, G.; Zan, G.; Li, J.; Lee, S. J.; Wang, Y.; Zhu, Y.; Gul, S.; Vine, D. J.; Lewis, S.; Yun, W.; Ma, Z. F.; Pianetta, P.; Lee, J. S.; Li, L.; Liu, Y. Structural, Dynamic, and Chemical Complexities in Zinc Anode of an Operating Aqueous Zn-Ion Battery. *Adv. Energy Mater.* **2022**, *12*, 2200255.

[6] Chen, R.; Zhang, C.; Li, J.; Du, Z.; Guo, F.; Zhang, W.; Dai, Y.; Zong, W.; Gao, X.; Zhu, J.; Zhao, Y.; Wang, X.; He, G. A hydrated deep eutectic electrolyte with finely-tuned solvation chemistry for high-performance zinc-ion batteries. *Energy Environ. Sci.* **2023**, *16*, 2540–2549.

[7] Wang, C.; Yang, H.; Wang, B.; Ding, P.; Wan, Y.; Bao, W.; Li, Y.; Ma, S.; Liu, Y.; Lu, Y.; Hu, H. Dual cation doping enabling simultaneously boosted capacity and rate capability of MnO_2 cathodes for Zn//MnO_2 batteries. *Nano Res.* **2023**, *16*, 9488–9495.

[8] Sun, W.; Wang, F.; Hou, S.; Yang, C.; Fan, X.; Ma, Z.; Gao, T.; Han, F.; Hu, R.; Zhu, M.; Wang, C. Zn/MnO_2 Battery Chemistry With H^+ and Zn^{2+} Coinsertion. *J. Am. Chem. Soc.* **2017**, *139*, 9775–9778.

[9] Liu, M.; Li, X.; Cui, M.; Chen, F.; Li, J.; Shi, W.; Liu, Y.; Li, X.; Wang, Y.; Zhang, W.; Shao, C.; Liu, Y. Amorphous organic-hybrid vanadium oxide for near-barrier-free ultrafast-charging aqueous zinc-ion battery. *Nat. Commun.* **2024**, *15*, 10769.

[10] Wang, Y.; Wei, S.; Qi, Z. H.; Chen, S.; Zhu, K.; Ding, H.; Cao, Y.; Zhou, Q.; Wang, C.; Zhang, P.; Guo, X.; Yang, X.; Wu, X.; Song, L. Intercalant-induced V t2g orbital occupation in vanadium oxide cathode toward fast-charging aqueous zinc-ion batteries. *Proc. Natl. Acad. Sci.* **2023**, *120*, e2217208120.

[11] Xie, Z. L.; Zhu, Y.; Du, J. Y.; Yang, D. Y.; Zhang, N.; Sun, Q. Q.; Huang, G.; Zhang, X. B. Reconfiguring the Hydrogen Networks of Aqueous Electrolyte to Stabilize Iron Hexacyanoferrate for High-Voltage pH-Decoupled Cell. *Angew. Chem., Int. Ed.* **2024**, *63*, e202400916.

[12] Chao, D.; Zhou, W.; Ye, C.; Zhang, Q.; Chen, Y.; Gu, L.; Davey, K.; Qiao, S. Z. An Electrolytic Zn–MnO_2 Battery for High-Voltage and Scalable Energy Storage. *Angew. Chem., Int. Ed.* **2019**, *58*, 7823–7828.

[13] Zeng, X.; Liu, J.; Mao, J.; Hao, J.; Wang, Z.; Zhou, S.; Ling, C. D.; Guo, Z. Toward a Reversible Mn^{4+}/Mn^{2+} Redox Reaction and Dendrite-Free Zn Anode in Near-Neutral Aqueous Zn/MnO_2 Batteries via Salt Anion Chemistry. *Adv. Energy Mater.* **2020**, *10*, 1904163.

[14] Song, C.; Gong, Z.; Bai, C.; Cai, F.; Yuan, Z.; Liu, X. High performance $Zn–I_2$ battery with acetonitrile electrolyte working at low temperature. *Nano Res.* **2021**, *15*, 3170–3177.

[15] Deng, Y.; Wang, H.; Fan, M.; Zhan, B.; Zuo, L. J.; Chen, C.; Yan, L. Nanomicellar Electrolyte To Control Release Ions and Reconstruct Hydrogen Bonding Network for Ultrastable High-Energy-Density Zn–Mn Battery. *J. Am. Chem. Soc.* **2023**, *145*, 20109–20120.

[16] Wang, K.; Li, H.; Xu, Z.; Liu, Y.; Ge, M.; Wang, H.; Zhang, H.; Lu, Y.; Liu, J.; Zhang, Y.; Tang, Y.; Chen, S. An Iodine-Chemisorption Binder for High-Loading and Shuttle-Free Zn–Iodine Batteries. *Adv. Energy Mater.* **2024**, *14*, 2304110.

[17] He, J.; Mu, Y.; Wu, B.; Wu, F.; Liao, R.; Li, H.; Zhao, T.; Zeng, L. Synergistic effects of Lewis acid-base and Coulombic interactions for high-performance $Zn–I_2$ batteries. *Energy Environ. Sci.* **2024**, *17*, 323–331.

[18] Zhong, W.; Cheng, H.; Zhang, S.; Li, L.; Tan, C.; Chen, W.; Lu, Y. Cation-driven phase transition and anion-enhanced kinetics for high energy efficiency zinc-interhalide complex batteries. *Nat. Commun.* **2025**, *16*, 4586.

[19] Li, X.; Li, M.; Huang, Z.; Liang, G.; Chen, Z.; Yang, Q.; Huang, Q.; Zhi, C. Activating the I^0/I^+ redox couple in an aqueous I_2–Zn battery to achieve a high voltage plateau. *Energy Environ. Sci.* **2021**, *14*, 407–413.

[20] Xie, Y.; Pan, T.; Lei, Q.; Chen, C.; Dong, X.; Yuan, Y.; Shen, J.; Cai, Y.; Zhou, C.; Pinnau, I.; Han, Y. Ionic Functionalization of Multivariate Covalent Organic Frameworks to Achieve an Exceptionally High Iodine-Capture Capacity. *Angew. Chem., Int. Ed.* **2021**, *60*, 22432–22440.

[21] Hu, T.; Zhao, Y.; Yang, Y.; Lv, H.; Zhong, R.; Ding, F.; Mo, F.; Hu, H.; Zhi, C.; Liang, G. Development of Inverse-Opal-Structured Charge-Deficient Co_9S_8@nitrogen-Doped-Carbon to Catalytically Enable High Energy and High Power for the Two-Electron Transfer I^+/I^- Electrode. *Adv. Mater.* **2024**, *36*, 2312246.

[22] Zhang, P. F.; Ma, M. M.; Wu, X.; Chu, W. W.; Xu, S. L.; Su, H. X.; Du, F. H.; Liu, L. Y.; Kong, X. J.; Li, H. X.; Ding, L.; Wang, Z. Y.; Li, Z. G.; Zhou, Y.; Zhang, S. J.; Wang, Y.; Zhen, C. h.; Li, J. T. Relocating Conjugated 2P Valence Electrons in Carbon Host to Stabilize I^+ for Novel Zn–I_2 Battery. *Adv. Energy Mater.* **2025**, *15*, 2404845.

[23] Zou, Y.; Liu, T.; Du, Q.; Li, Y.; Yi, H.; Zhou, X.; Li, Z.; Gao, L.; Zhang, L.; Liang, X. A four-electron Zn–I_2 aqueous battery enabled by reversible $I^-/I_2/I^+$ conversion. *Nat. Commun.* **2021**, *12*, 170.

[24] Rao, S.; Song, W.; Lu, Z.; Ma, Q.; Ye, L.; Fujishige, M.; Takeuchi, K.; Endo, M.; Niu, J.; Wang, F. Carbon nanofiber embedded with amorphous VO_x as a functional framework for Zn anode modification. *Nano Res.* **2025**, *18*, 94907588.

[25] Lv, Y.; Huang, C.; Zhao, M.; Fang, M.; Dong, Q.; Tang, W.; Yang, J.; Zhu, X.; Qiao, X.; Zheng, H.; Sun, C.; Zheng, L.; Zheng, M.; Xu, Y.; Lu, J. Synergistic Anion–Cation Chemistry Enables Highly Stable Zn Metal Anodes. *J. Am. Chem. Soc.* **2025**, *147*, 8523–8533.

[26] Qiu, Y.; Lin, Y.; Shi, D.; Zhang, H.; Luo, J.; Chen, J.; Liu, Z.; Yu, Y.; Lin, D.; Zhang, W.; Li, Y.; Yang, C. Möbius Solvation Structure for Zinc-Ion Batteries. *Adv. Mater.* **2025**, *37*, 2415373.

[27] Liu, Z.; Wang, R.; Gao, Y.; Zhang, S.; Wan, J.; Mao, J.; Zhang, L.; Li, H.; Hao, J.; Li, G.; Zhang, L.; Zhang, C. Low-Cost Multi-Function Electrolyte Additive Enabling Highly Stable Interfacial Chemical Environment for Highly Reversible Aqueous Zinc Ion Batteries. *Adv. Funct. Mater.* **2023**, *33*, 2308463.

[28] Jiang, P.; Du, Q.; Lei, C.; Xu, C.; Liu, T.; He, X.; Liang, X. Stabilized four-electron aqueous zinc–iodine batteries by quaternary ammonium complexation. *Chem Sci* **2024**, *15*, 3357–3364.

[29] Wang, Y.; Zhao, R.; Liu, M.; Yang, J.; Zhang, A.; Yue, J.; Wu, C.; Bai, Y. Suppressed Water Reactivity by Zincophilic-Hydrophobic Electrolyte Additive for Superior Aqueous Zn Metal Batteries. *Adv. Energy Mater.* **2023**, *13*, 2302707.

[30] Zhu, Y.; Chen, Q.; Hao, J.; Jiao, Y. Breaking hydrogen-bonds in aqueous electrolytes towards highly reversible zinc-ion batteries. *J. Mater. Chem. A* **2024**, *12*, 20097–20106.

[31] Yang, Q.; Guo, L.; Liu, Z.; Wang, J.; Luo, H.; Zhang, X.; He, Q.; Chen, X.; Li, M.; Wang, Z.; Jiang, Y.; Yuan, R.; Liu, Z.; Zhang, K.; Hu, Z.; Huang, Y. Regulation of Zn^{2+} desolvation kinetics via interfacial hydrogen-bond network for a highly reversible Zn metal anode. *Energy Storage Mater.* **2025**, *75*, 104028.

[32] Meng, Q.; Bai, Q.; Zhao, R.; Cao, P.; Zhang, G.; Wang, J.; Su, F.; Zhou, X.; Yang, J.; Tang, J. Attenuating Water Activity Through Impeded Proton Transfer Resulting from Hydrogen Bond Enhancement Effect for Fast and Ultra-Stable Zn Metal Anode. *Adv. Energy Mater.* **2023**, *13*, 2302828.

[33] Ren, B.; Hu, S.; Chen, A.; Zhang, X.; Wei, H.; Jiang, J.; Chen, G.; Zhi, C.; Li, H.; Liu, Z. Inhibiting Dendrite Formation and Electrode Corrosion via a Scalable Self-Assembled Mercaptan Layer for Stable Aqueous Zinc Batteries. *Adv. Energy Mater.* **2023**, *14*, 2302970.

[34] Chen, Y.; He, W.; Zhao, K.; Luo, X.; Zhang, J.; Wu, Y.; Hao, X. Constructing Compact Hybrid Buffer Interface via Ion Agglomeration Zone Electrolyte for Stable Zn Metal Battery. *Adv. Energy Mater.* **2025**, *16*, 2405738.

[35] Xiao, Z.; Dai, X.; Zhu, J.; Liu, D.; Liu, L.; Liu, X.; Li, Y.; Qian, Z.; Wang, R. Hydrogen Bond Competition Optimizing Aqueous Zn Ion Solvation and (002) Interfacial Deposition with Ultralong Stability. *Adv. Funct. Mater.* **2025**, *35*, 2424860.

[36] Heo, J.; Shin, K.; Kim, H. T. A Zinc-Bromine Battery with Deep Eutectic Electrolytes. *Adv. Sci.* **2022**, *9*, e2204908.

[37] Gao, L.; Li, Z.; Zou, Y.; Yin, S.; Peng, P.; Shao, Y.; Liang, X. A High-Performance Aqueous Zinc–Bromine Static Battery. *Iscience* **2020**, *23*, 101348.

[38] Xie, C.; Wang, C.; Xu, Y.; Li, T.; Fu, Q.; Li, X. Reversible multielectron transfer I^-/IO_3^- cathode enabled by a hetero-halogen electrolyte for high-energy-density aqueous batteries. *Nat. Energy* **2024**, *9*, 714–724.

[39] Wang, C.; Ji, X.; Liang, J.; Zhao, S.; Zhang, X.; Qu, G.; Shao, W.; Li, C.; Zhao, G.; Xu, X.; Li, H. Activating and Stabilizing a Reversible four Electron Redox Reaction of I^-/I^+ for Aqueous Zn–Iodine Battery. *Angew. Chem., Int. Ed.* **2024**, *63*, e202403187

[40] Wang, M.; Meng, Y.; Sajid, M.; Xie, Z.; Tong, P.; Ma, Z.; Zhang, K.; Shen, D.; Luo, R.; Song, L.; Wu, L.; Zheng, X.; Li, X.; Chen, W. Bidentate Coordination Structure Facilitates High-Voltage and High-Utilization Aqueous Zn–I_2 Batteries. *Angew. Chem., Int. Ed*. **2024**, *63*, e202404784.

[41] Yin, Y.; Yuan, Z.; Li, X. Rechargeable aqueous zinc-bromine batteries: an overview and future perspectives. *Phys Chem Chem Phys* **2021**, *23*, 26070–26084.

[42] Lv, S.; Fang, T.; Ding, Z.; Wang, Y.; Jiang, H.; Wei, C.; Zhou, D.; Tang, X.; Liu, X. A High-Performance Quasi-Solid-State Aqueous Zinc–Dual Halogen Battery. *ACS Nano* **2022**, *16*, 20389–20399.

[43] Han, W.; Zhao, J.; Li, X. Ternary chloride-free electrolyte design for highly efficient aqueous zinc–iodine batteries with four-electron conversion. *Inorg. Chem. Front.* **2024**, *11*, 5376–5383.

[44] Sun, Q. Q.; Sun, T.; Du, J. Y.; Li, K.; Xie, H. M.; Huang, G.; Zhang, X. B. A Sulfur Heterocyclic Quinone Cathode Towards High-Rate and Long-Cycle Aqueous Zn-Organic Batteries. *Adv. Mater.* **2023**, *35*, 2301088.

[45] Sun, Q. Q.; Sun, T.; Du, J. Y.; Xie, Z. L.; Yang, D. Y.; Huang, G.; Xie, H. M.; Zhang, X. B. In Situ Electrochemical Activation of Hydroxyl Polymer Cathode for High-Performance Aqueous Zinc–Organic Batteries. *Angew. Chem. Int., Ed.* **2023**, *62*, e202307365.

[46] Zhang, L.; Han, Y.; Geng, Y.; Zhang, H.; Liu, H.; He, Y.; Yan, Z.; Zhu, Z. Aqueous Zinc-Ion Batteries with Boosted Stability and Kinetics under a Wide Temperature Range. *Angew. Chem., Int. Ed.* **2025**, *64*, e202500434.

Electronic Supplementary Material

"Dual-side shielding": Bromide additives enabling robust four-electron aqueous Zn–I_2 batteries

Zhenbang Zhuang[1,2], Jun Guo[2], Chunling Chen[2,3], Junmin Yan[1], Gang Huang[2,3] ✉, and Xinbo Zhang[2,3] ✉

[1] *Key Laboratory of Automobile Materials, Ministry of Education, Department of Materials Science and Engineering, Jilin University, Changchun 130022, China*
[2] *China-Belarus Belt and Road Joint Laboratory on Advanced Materials and Manufacturing, Changchun Institute of Applied Chemistry, Chinese Academy of Sciences, Changchun 130022, China*
[3] *School of Applied Chemistry and Engineering, University of Science and Technology of China, Hefei 230026, China*

✉ Address correspondence to Gang Huang, ghuang@ciac.ac.cn; Xinbo Zhang, xbzhang@ciac.ac.cn

Supporting information to https://doi.org/10.26599/NR.2026.94908914

Experimental

1 Materials

Zn foil (0.038 mm thick, > 99%) from SCI Materials Hub was used as anodes and Kochen Black (KB) (ECP-600JD) conductive agent was provided from Japan. Carbon nanotube (CNT) was purchased from NanJing Suzhan Company (> 95%, 1–2 nm in diameter). $ZnSO_4 \cdot 7H_2O$ (99.99%) was bought from Macklin reagent. $ZnBr_2$ (> 99.9%), iodine (I_2, 99%), and trimethylammonium bromide ($C_3H_9N \cdot HBr$, TMBr, > 98%) were supplied by Aladdin. Ti mesh (100 mesh) was obtained from Kang Wei Company. Glass fiber membranes (GF/D and GF/A) were purchased from Whatman. 1-methyl-1-ethylpyrrolidinium bromide (PBr) was obtained from Qingdao Aoli New Materials Company. Tetraethylammonium bromide (TEBr) was bought from TCI Reagents. Unless the above specified, all other reagents and chemicals were purchased from Xilong Science.

2 Preparation of solutions

ZSO-$ZnBr_2$, ZSO-TEBr, ZSO-PBr, and ZSO-TBBr solutions were respectively synthesized by adding 1.25 mmol $ZnBr_2$, 1.2 mmol TEBr, 2.5 mmol PBr, and 1 mmol TBBr into 5 mL 2 M ZSO electrolyte.

3 Materials Characterizations

Nuclear magnetic resonance (NMR) spectra were carried out on a Bruker Avance III 500 MHz instrument, and D_2O was used as the inner standard solvent to test ^{1}H-NMR. Nicolet 6700 spectrometer with a mode of Attenuated Total Refraction (ATR) was used to conduct the Fourier transform infrared spectra (FTIR) test. Raman characterization was performed on a T64000 device with an excitation laser of 532 nm. Powder X-ray diffraction (XRD) test was conducted on a Rigaku MiniFlex 600 X-ray diffractometer. X-ray photoelectron spectra (XPS) were executed by an ESCALABMKII X-ray photoelectron spectrometer using an Al Kα source. Structure and element analysis of electrodes was studied by a scanning electron microscope (SEM, S-4800) with energy dispersive X-ray spectrometer. TU–1900 measurement instrument with ultraviolet-visible spectrometer (UV–vis spectrum) was used to inspect the change of absorbance.

4 Computational Details

DFT simulations were performed using the freely available CP2K/Quickstep package[1]. Vacuum>20 Å was added to both surfaces to eliminate the interactions between images. The Perdew–Burke–Ernzerhof (PBE) density functional with the Grimme D3 dispersion correction was used[2-4]. The core electrons were represented by Goedecker-Teter-Hutter (GTH) pseudopotentials[5]. The Gaussian basis set was double-ζwith one set of polarization functions (DZVP-MOLOPT-SR-GTH)[6, 7], and the plane wave cutoff was set to 400 Ry. The geometries were optimized by Broyden-Fletcher-Goldfarb-Shanno (BFGS) minimizer. For molecular dynamics, OPLS-AA force field[8] was generated to describe water and TMBr molecules. Open source Large-scale Atomic/Molecular Massively Parallel Simulator (LAMMPS)[9] was applied to drive molecular dynamics calculation. NpT ensemble was applied with the temperature set to 300 K and pressure set to 1 bar. NpT ensembles were used with the Nose-Hoover thermostat for temperature controlling and Parinello-Rahman barostat for pressure controlling. Initial configurations were constructed according to the experiments and

pre-equilibrated with 300 ps NVT and 700 ps NpT simulation. About 1 ns trajectory was generated to compute the RDF and Hydrogen Bonds.

5 Electrochemical Characterizations

CR2025 coin batteries were assembled to conduct electrochemistry performance tests. The Zn–I_2 full batteries were assembled by utilizing Zn foil (Φ = 12 mm), glass fiber (GF/D, Φ = 16 mm), 2 M $ZnSO_4$/2 M $ZnSO_4$ + 0.5 M TMBr (ZSO/ZSO-TMBr), and SSCC/I_2 as anode, separator, electrolyte, and cathode. For Zn||Zn symmetrical and Zn||Cu asymmetrical batteries, Zn foil and Cu foil were used as the cathode, respectively, and Swagelok type cells were used as their battery devices. The pouch cell mainly consisted of two pieces of cathodes (one piece size: 60 × 80 mm^2, I_2 loading: 5.7 mg cm^{-2}, total mass = 550 mg), ZSO-TMBr electrolyte, glass fiber membrane (GF/A, 65 × 85 mm^2), and Zn foil (60 × 80 mm^2), and vacuum sealed by aluminum-plastic film. Cycling performance, galvanostatic charge-discharge curves, and rate performance were studied by a LANDt (CT3001A) battery test system. BioLogic VMP-300 electrochemistry station was used to measure cyclic voltammetry (CV) curves, linear sweep voltammetry (LSV), chronoamperometry (I–t) curves, Tafel plots (TP), and electrochemical impedance spectroscopy (EIS). CV curves were tested at 0.1, 0.3, 0.5, 0.7, and 1 mV s^{-1} from 0.6 ~ 1.6 V, and EIS were performed in the frequency range from 7 MHz to 100 mHz with an amplitude of 10 mV. LSV, TP, and I–t curves of Zn||Zn symmetrical batteries were tested at 1 mV s^{-1}, 10 mV min^{-1}, and −150 mV.

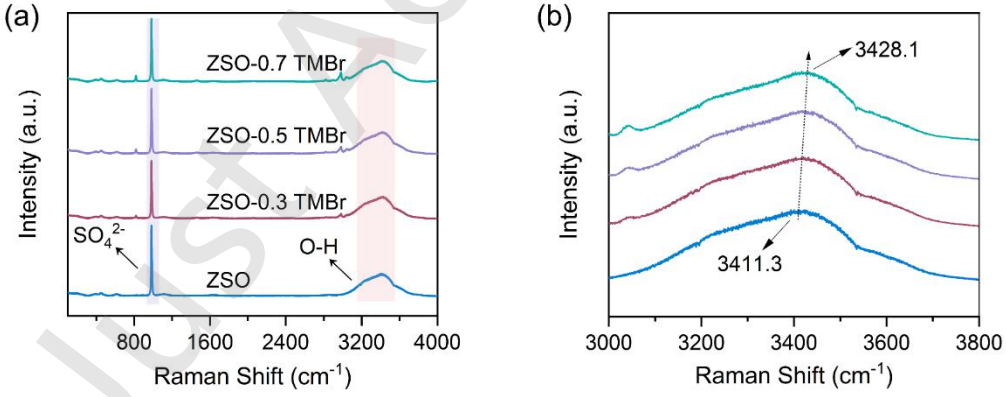

Figure S1. Raman spectra of (a) ZSO with different concentrations of TMBr and (b) zoom in details around the –OH location.

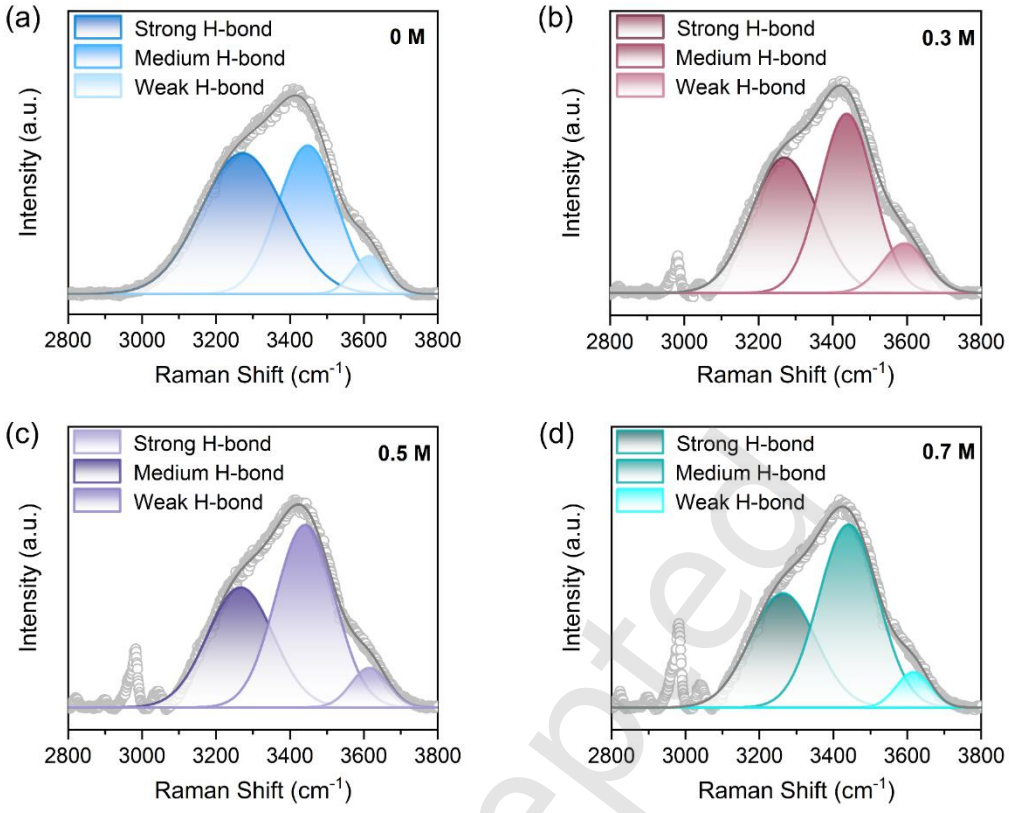

Figure S2. The fitting Raman spectra around the –OH location: (a) ZSO, (b) ZSO-0.3 TMBr, (c) ZSO-0.5 TMBr, and (d) ZSO-0.7 TMBr electrolytes.

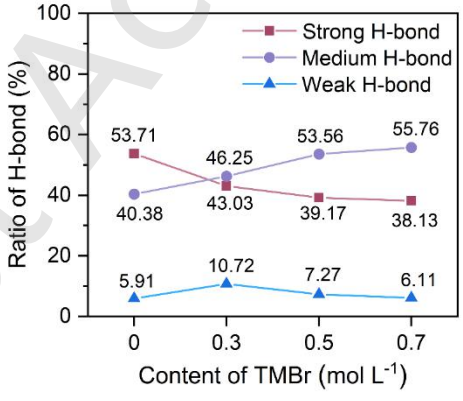

Figure S3. Different-type H-bond ratio of ZSO containing different contents of TMBr.

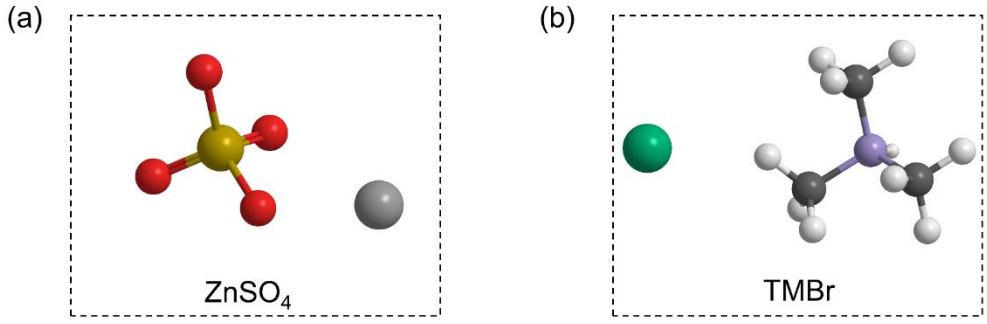

Figure S4. Structure models of (a) $ZnSO_4$ and (b) TMBr.

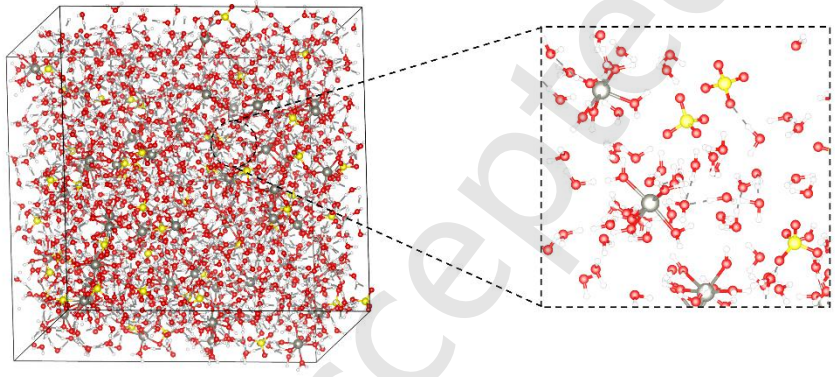

Figure S5. MD simulation models of ZSO electrolyte and counterpart on partial enlarged details.

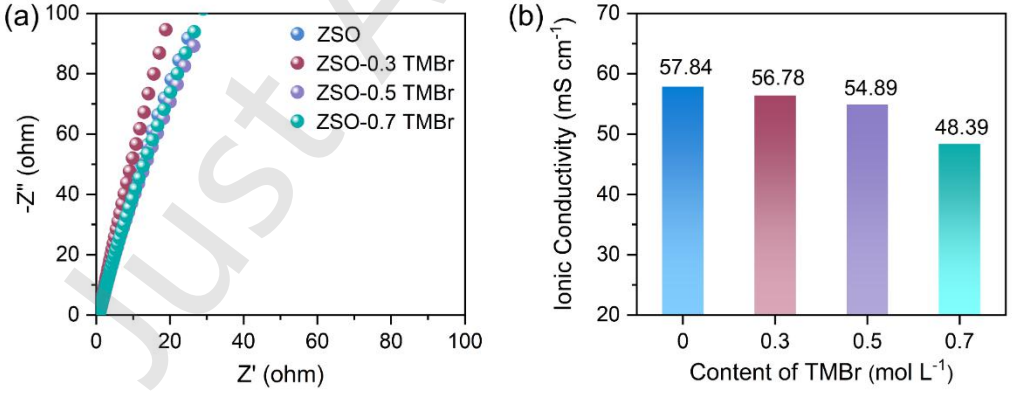

Figure S6. (a) EIS of stainless-steel symmetrical cells and (b) ionic conductivity of ZSO containing different contents of TMBr.

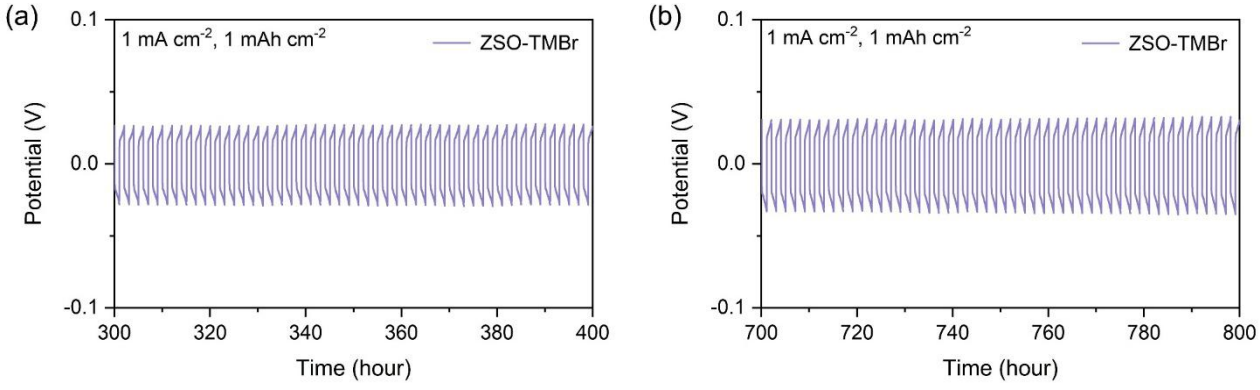

Figure S7. The partial enlarged details on cycling performance of Zn||Zn symmetrical batteries at (a, b) 1 mA cm^{-2}/1 mAh cm^{-2} and (c, d) 5 mA cm^{-2}/5 mAh cm^{-2}.

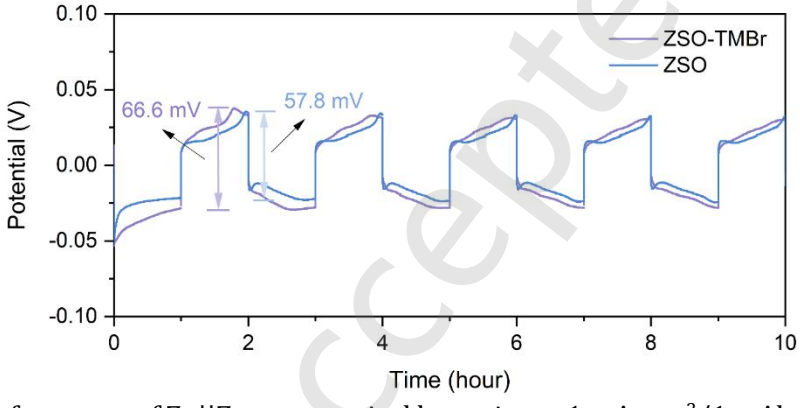

Figure S8. Cycling performance of Zn||Zn symmetrical batteries at 1 mA cm^{-2}/1 mAh cm^{-2} for the first 5th cycles.

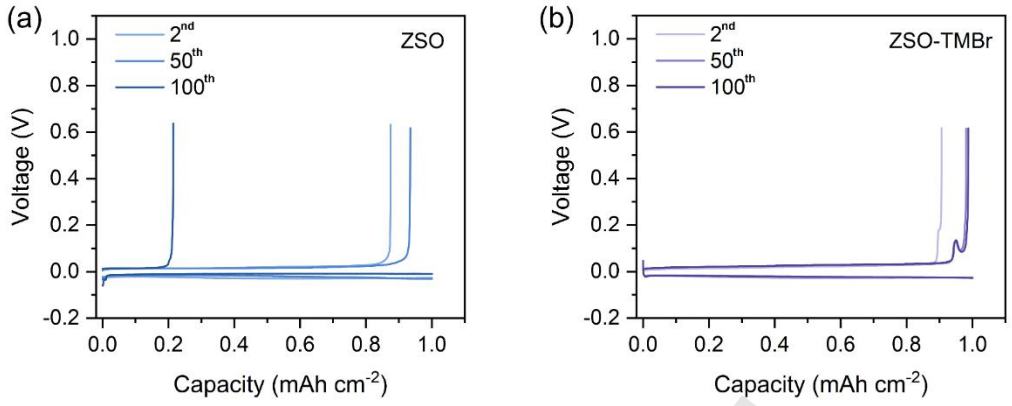

Figure S9. Charge-discharge profiles of Zn||Cu cells with (a) ZSO and (b) ZSO-TMBr electrolytes at 1 mA cm^{-2}/1 mAh cm^{-2} for the 2nd, 50th, and 100th cycle.

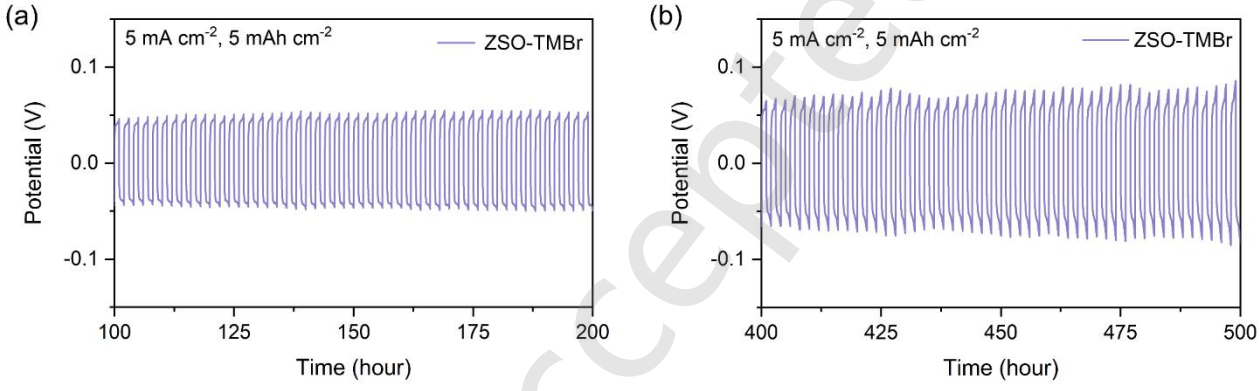

Figure S10. The partial enlarged details on cycling performance of Zn||Zn symmetrical batteries at (a, b) 5 mA cm^{-2}/5 mAh cm^{-2}.

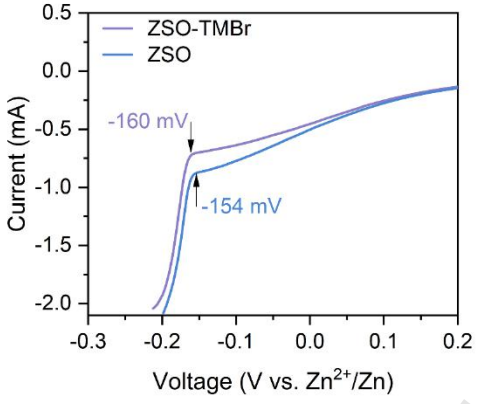

Figure S11. Linear sweep voltammetry (LSV) of Zn||Zn cells with ZSO and ZSO-TMBr electrolytes at 1 mV s^{-1}.

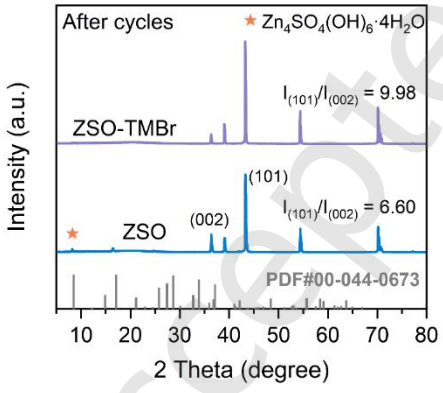

Figure S12. XRD patterns of Zn anodes after 20 cycles in ZSO and ZSO-TMBr electrolytes.

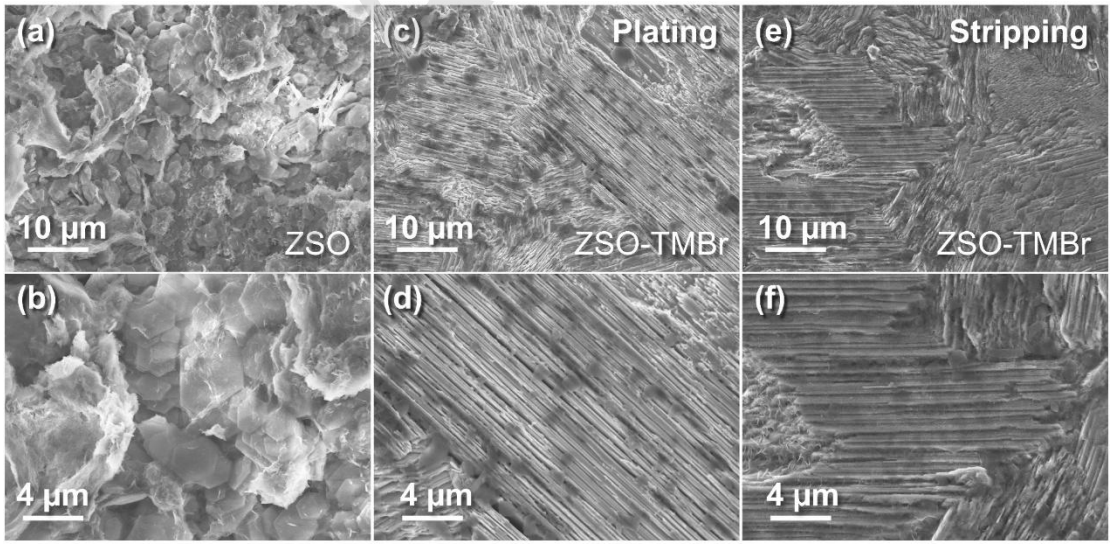

Figure S13. SEM images of Zn anodes after 50 cycles of Zn||Zn symmetric cells with (a, b) ZSO and (c–f) ZSO-TMBr electrolytes.

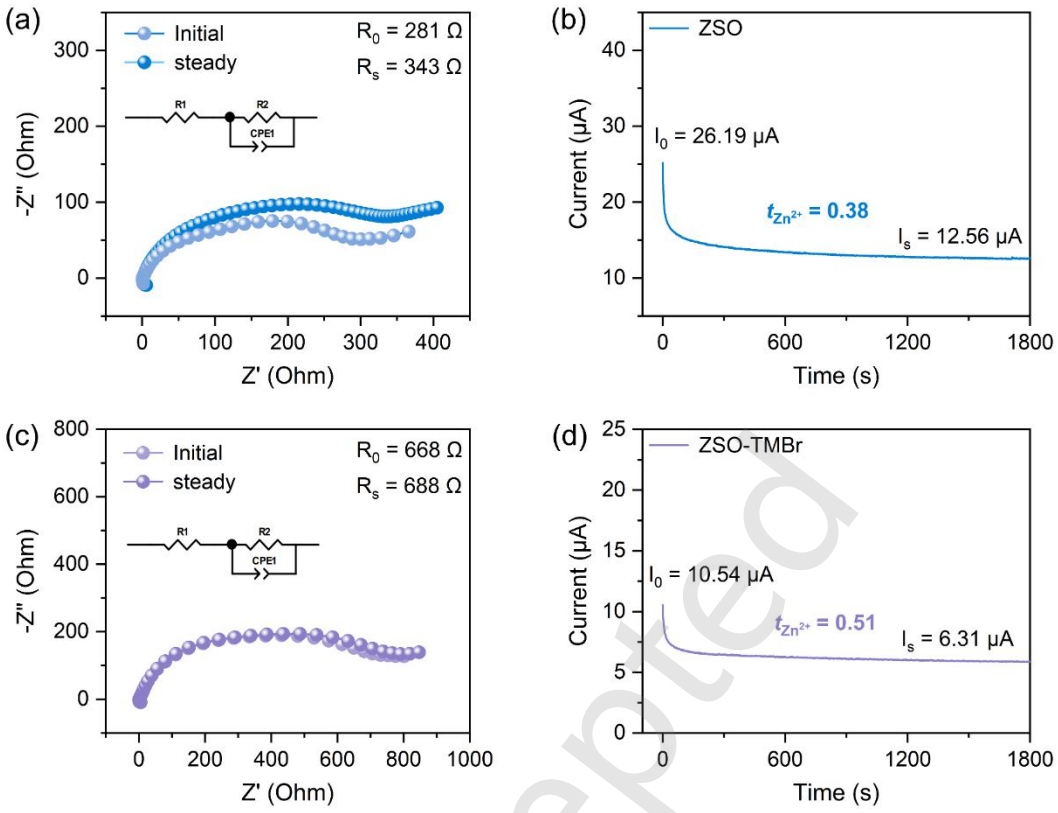

Figure S14. EIS of Zn||Zn symmetric cells with (a) ZSO and (c) ZSO-TMBr electrolytes. I–t plots in (b) ZSO and (d) ZSO-TMBr electrolytes at a constant voltage of 20 mV for 1800 s.

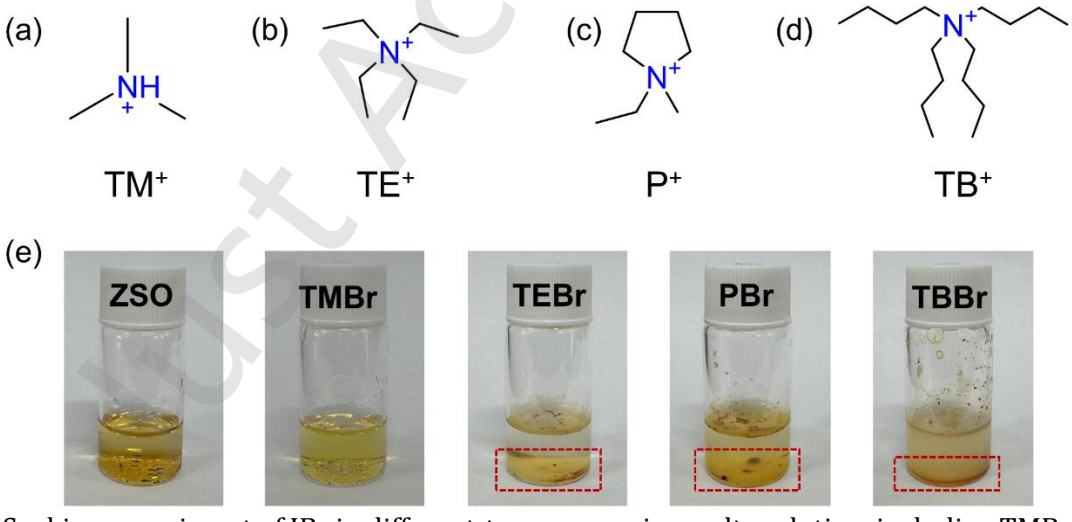

Figure S15. Soaking experiment of IBr in different-type ammonium salts solution, including TMBr, TEBr, PBr, and TBBr. (a–d) Corresponding cation structures and (e) optical photos.

The part enclosed by the dotted line is the fluffy sediment formed at the bottom. The cloudy substance indicates that precipitation is forming. The presence of black specks at the bottom of the container is not yet completely reacted IBr due to the short soaking period (5 min).

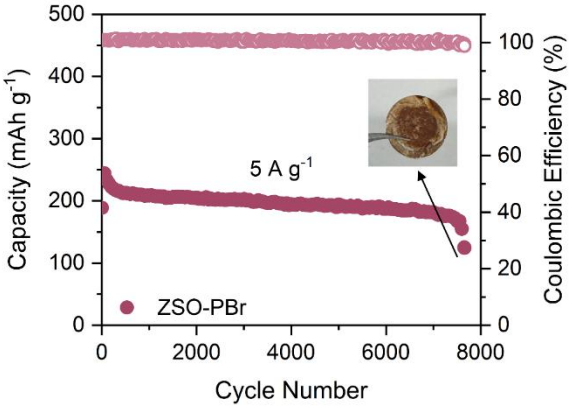

Figure S16. Cycling performance of Zn–I_2 batteries with 2 M $ZnSO_4$-0.5 M PBr (ZSO-PBr) electrolyte. Inset is the cathode after finishing cycles.

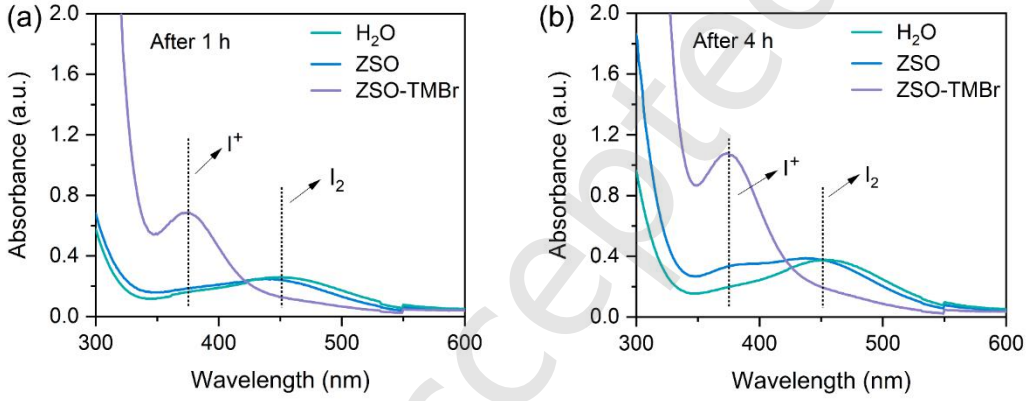

Figure S17. UV–vis spectra of 10 mg IBr immersing in H_2O, ZSO and ZSO-TMBr solution after (a) 1 h and (b) 4 h.

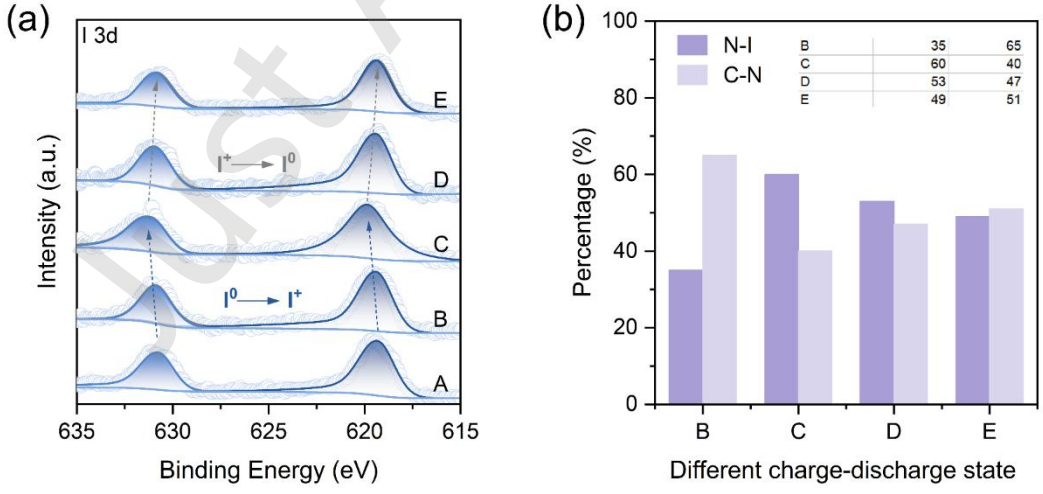

Figure S18. (a) I 3d fine spectra of ex situ XPS at different charge-discharge states; (b) The percentage of N-I and C-N content at different charge-discharge state.

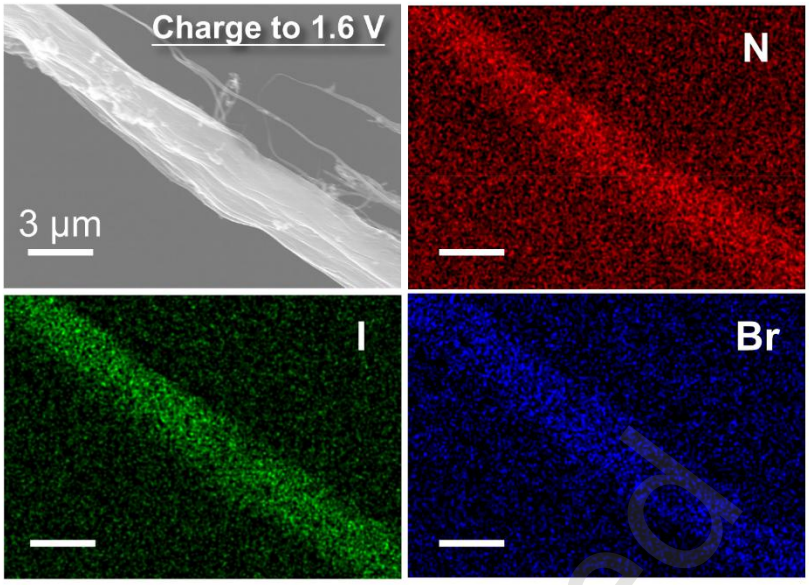

Figure S19. SEM and corresponding EDS-mapping images of I_2 cathode charged to 1.6 V in ZSO-TMBr electrolyte.

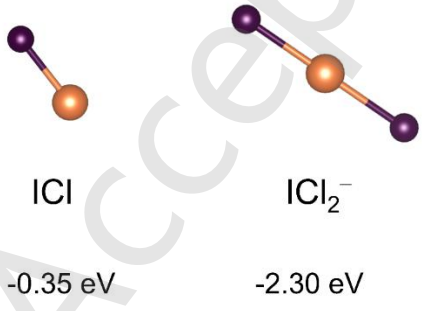

Figure S20. Binding energy of ICl and ICl_2^-.

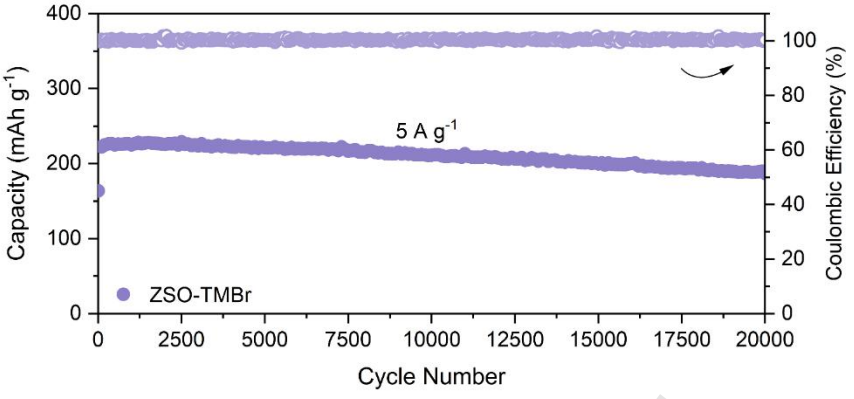

Figure S21. Cycling performance of Zn–I_2 battery with ZSO-TMBr electrolyte at 5 A g^{-1}.

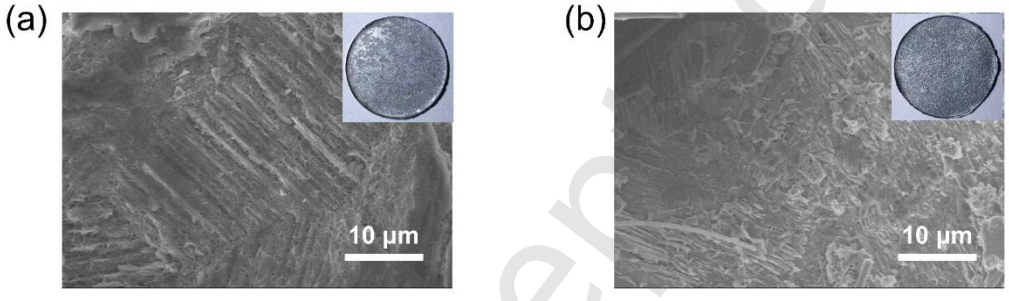

Figure S22. Optical photos and SEM images of Zn anodes after (a) 100 and (b) 1000 cycles in Zn–I_2 batteries.

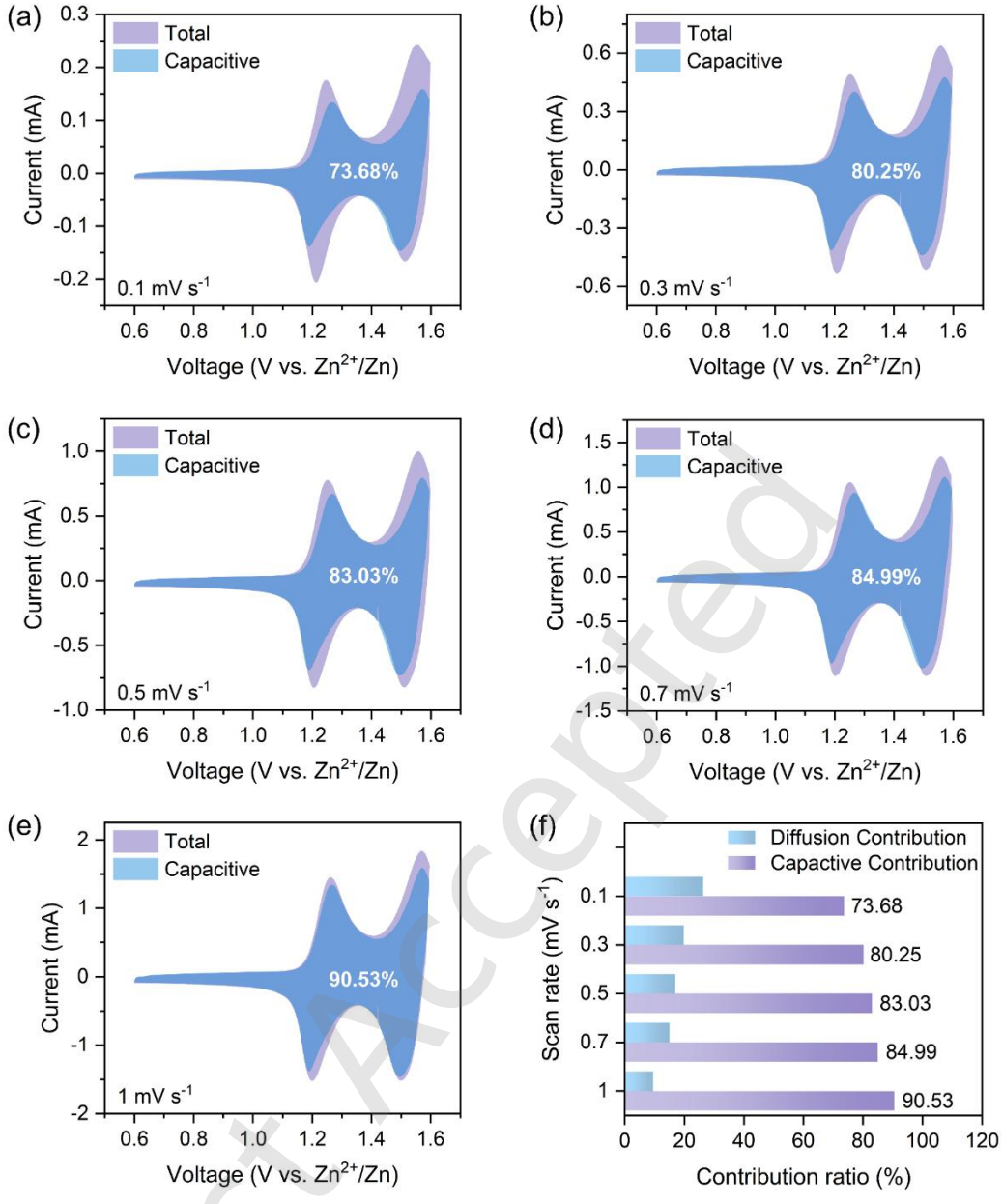

Figure S23. Simulative capacitive contributions at scan rates of (a) 0.1, (b) 0.3, (c) 0.5, (d) 0.7, and (e) 1 mV s^{-1}, and (f) statistical histogram of calculated contribution ratio.

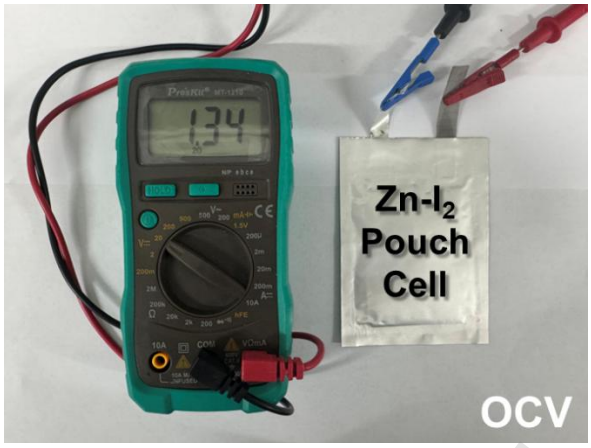

Figure S24. Open circuit voltage (OCV) of Zn–I_2 pouch cell.

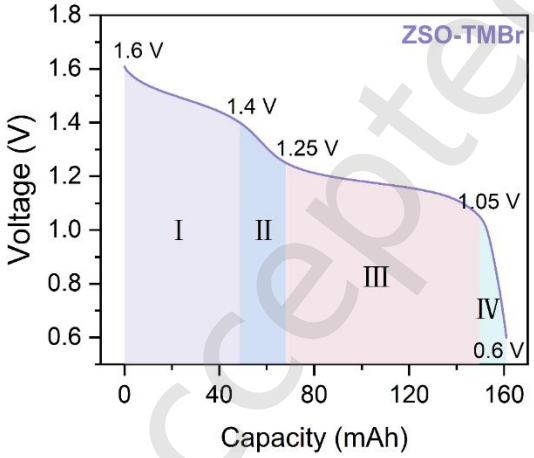

Figure S25. The four regions' divisions of the discharge process of the pouch cell.

We have divided the discharge process into four distinct areas: I, II, III and IV. Their average voltage is calculated as the average of the highest and lowest voltages in the corresponding area. The voltages and capacities of the four areas are shown in the table below. Here, the average voltage and capacity are abbreviated as V_{avg} and C:

	I	II	III	IV
V_{avg} (V)	1.50	1.33	1.15	0.83
C (mAh)	48.60	19.50	81.60	11.30

According to the calculation formula of energy density (E): $E = \sum(C \times V_{avg})/m$,
E = (1.50×48.60+1.33×19.50+1.15×81.60+0.83×11.30) ×10^{-3} Wh/ (550×10^{-6}) kg = 367.4 Wh kg^{-1}

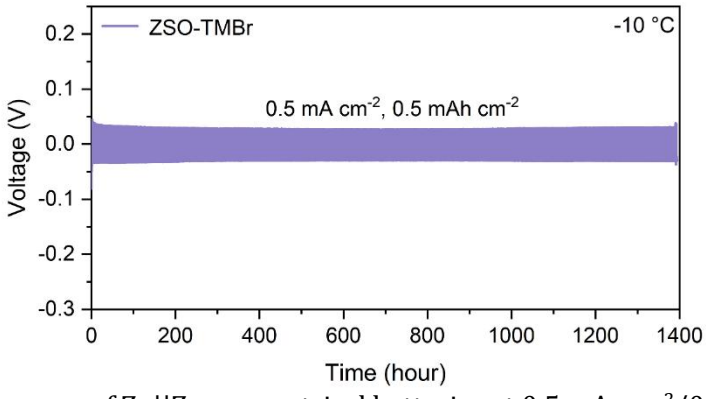

Figure S26. Cycling performance of Zn||Zn symmetrical batteries at 0.5 mA cm^{-2}/0.5 mAh cm^{-2} and −10 °C.

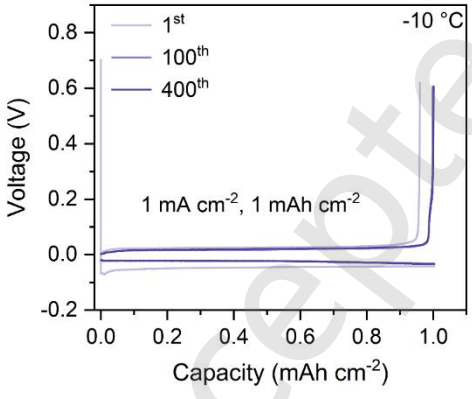

Figure S27. Charge-discharge profiles of Zn||Cu cells at −10 °C for the 1st, 100th, and 400th cycle.

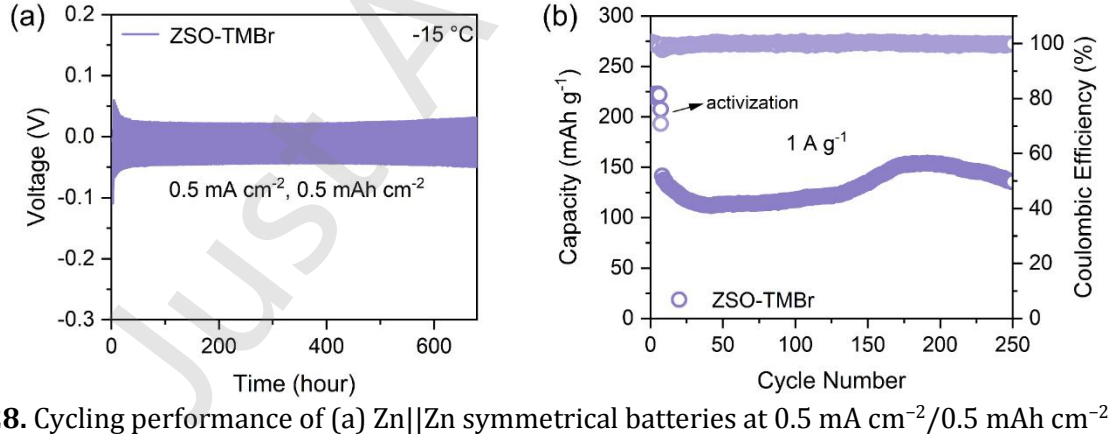

Figure S28. Cycling performance of (a) Zn||Zn symmetrical batteries at 0.5 mA cm^{-2}/0.5 mAh cm^{-2} and (b) Zn–I_2 batteries at 1 A g^{-1} and −15 °C.

Table S1. H-bond number per H_2O molecule in ZSO electrolyte.

2 M $ZnSO_4$	Number of H-bond	H-bond donor	H-bond acceptor
$OH–OH_2$	0.802	H_2O	H_2O
$HO–H_2O$	1.603	H_2O	H_2O
$OH–SO_4^{2-}$	0.266	H_2O	SO_4^{2-}

Table S2. H-bond number per H_2O molecule in ZSO-TMBr electrolyte.

ZSO-TMBr	Number of H-bond	H-bond donor	H-bond acceptor
$OH–OH_2$	0.750	H_2O	H_2O
$HO–H_2O$	1.500	H_2O	H_2O
$OH–SO_4^{2-}$	0.218	H_2O	SO_4^{2-}
$OH–Br^-$	0.045	H_2O	Br^-
$HO–TM^+$	0.002	TM^+	H_2O

Table S3. Performance comparison of Zn–I_2 batteries with published literature.

Methods	Current density/A g^{-1}	Cycling number	Cycling time/h	Ref.
Ni–Fe–I/ZSO-$ZnBr_2$	10	10,000	400	[10]
ZSO-TAH	2	5,000	2,000	[11]
HC-SiO_2/21 m LiCl	0.422	400	606	[12]
ZSO-PyCl	10	10,000	600	[13]
O-B-C-N	8	9,000	675	[14]
ZSO/NaCl-0.2 HMTA	4	5,000	750	[15]
ZSO-TMBr	3	**15,000**	**2,400**	**This work**

References

[1] VandeVondele, J.; Krack, M.; Mohamed, F.; Parrinello, M.; Chassaing, T.; Hutter, J. Quickstep: Fast and accurate density functional calculations using a mixed Gaussian and plane waves approach. *Comput. Phys. Commun.* **2005**, *167*, 103–128.

[2] P. Perdew, J.; Burke, K.; Ernzerhof, M. Generalized Gradient Approximation Made Simple. *Phys. Rev. Lett* **1996**, *77*, 3865–3868.

[3] G. Kresse; Joubert, D. From Ultrasoft Pseudopotentials to the Projector Augmented-Wave Method. *Phys. Rev. B* **1999**, *59*, 1758–1775.

[4] Moellmann, J.; Grimme, S. DFT-D3 Study of Some Molecular Crystals. *J. Phys. Chem. C* **2014**, *118*, 7615–7621.

[5] VandeVondele, J.; Hutter, J. Gaussian basis sets for accurate calculations on molecular systems in gas and condensed phases. *J. Chem. Phys.* **2007**, *127*, 114105.

[6] S. Goedecker; M. Teter; Hutter, J. Separable dual-space Gaussian pseudopotentials. *Phys. Rev. B* **1996**, *54*, 1703–1710.

[7] C. Hartwigsen; S. Goedecker; Hutter, J. Relativistic separable dual-space Gaussian pseudopotentials from H to Rn. *Phys. Rev. B* **1998**, *58*, 3641–3662.

[8] Robertson, M. J.; Tirado-Rives, J.; Jorgensen, W. L. Improved Peptide and Protein Torsional Energetics with the OPLS-AA Force Field. *J. Chem. Theory Comput.* **2015**, *11*, 3499–3509.

[9] Thompson, A. P.; Aktulga, H. M.; Berger, R.; Bolintineanu, D. S.; Brown, W. M.; Crozier, P. S.; in 't Veld, P. J.; Kohlmeyer, A.; Moore, S. G.; Nguyen, T. D.; Shan, R.; Stevens, M. J.; Tranchida, J.; Trott, C.; Plimpton, S. J. LAMMPS - a flexible simulation tool for particle-based materials modeling at the atomic, meso, and continuum scales. *Comput. Phys. Commun.* **2022**, *271*, 108171.

[10] Wang, C.; Ji, X.; Liang, J.; Zhao, S.; Zhang, X.; Qu, G.; Shao, W.; Li, C.; Zhao, G.; Xu, X.; Li, H. Activating and Stabilizing a Reversible four Electron Redox Reaction of I^-/I^+ for Aqueous Zn–Iodine Battery. *Angew. Chem., Int. Ed.* **2024**, *63*, e202403187

[11] Wang, M.; Meng, Y.; Sajid, M.; Xie, Z.; Tong, P.; Ma, Z.; Zhang, K.; Shen, D.; Luo, R.; Song, L.; Wu, L.; Zheng, X.; Li, X.; Chen, W. Bidentate Coordination Structure Facilitates High-Voltage and High-Utilization Aqueous Zn–I_2 Batteries. *Angew. Chem., Int. Ed.* **2024**, *63*, e202404784.

[12] Chen, M.; Chen, G.; Sun, C.; Li, X.; Zhang, M.; Hua, H.; Zhao, J.; Yang, Y. SiO_2 Nanoparticles-Induced Antifreezing Hydrogel Electrolyte Enables Zn–I_2 Batteries with Complete and Reversible Four-Electron-Transfer Mechanisms at Low Temperatures. *Angew. Chem., Int. Ed.* **2025**, *64*, e202502005.

[13] Ren, G.; Yang, J.; Wang, J.; Peng, H.; Sun, T.; Zhang, J.; Li, Z. Activating and stabilizing of four-electron zinc-iodine batteries via dual reaction strategy. *J. Colloid Interface Sci.* **2025**, *696*, 137821.

[14] Zhang, P. F.; Ma, M. M.; Wu, X.; Chu, W. W.; Xu, S. L.; Su, H. X.; Du, F. H.; Liu, L. Y.; Kong, X. J.; Li, H. X.; Ding, L.; Wang, Z. Y.; Li, Z. G.; Zhou, Y.; Zhang, S. J.; Wang, Y.; Zhen, C. h.; Li, J. T. Relocating Conjugated 2P Valence Electrons in Carbon Host to Stabilize I^+ for Novel Zn–I_2 Battery. *Adv. Energy Mater.* **2025**, *15*, 2404845.

[15] Zhang, S.; Hao, J.; Wu, H.; Chen, Q.; Hu, Y.; Zhao, X.; Qiao, S. Z. Coordination Chemistry toward Advanced Zn–I_2 Batteries with Four-Electron $I^-/I^0/I^+$ Conversion. *J. Am. Chem. Soc.* **2025**, *147*, 16350–16361.